2019

Chemical Design of Palladium-Based Nanoarchitectures for Catalytic Applications

Muhammad Iqbal
National Institute For Materials Science

Yusuf Valentino Kaneti
National Institute For Materials Science

Jeonghun Kim
University of Queensland, jhkim@uow.edu.au

Brian Yuliarto
Institute of Technology Bandung

Yong-Mook Kang
Dongguk University, dake1234@dongguk.edu

See next page for additional authors

Publication Details

Iqbal, M., Kaneti, Y. Valentino., Kim, J., Yuliarto, B., Kang, Y., Bando, Y., Sugahara, Y. & Yamauchi, Y. (2019). Chemical Design of Palladium-Based Nanoarchitectures for Catalytic Applications. Small, 15 (6), 1804378-1-1804378-27.

Chemical Design of Palladium-Based Nanoarchitectures for Catalytic Applications

Abstract
Palladium (Pd) plays an important role in numerous catalytic reactions, such as methanol and ethanol oxidation, oxygen reduction, hydrogenation, coupling reactions, and carbon monoxide oxidation. Creating Pd-based nanoarchitectures with increased active surface sites, higher density of low-coordinated atoms, and maximized surface coverage for the reactants is important. To address the limitations of pure Pd, various Pd-based nanoarchitectures, including alloys, intermetallics, and supported Pd nanomaterials, have been fabricated by combining Pd with other elements with similar or higher catalytic activity for many catalytic reactions. Herein, recent advances in the preparation of Pd-based nanoarchitectures through solution-phase chemical reduction and electrochemical deposition methods are summarized. Finally, the trend and future outlook in the development of Pd nanocatalysts toward practical catalytic applications are discussed.

Disciplines
Engineering | Physical Sciences and Mathematics

Publication Details
Iqbal, M., Kaneti, Y. Valentino., Kim, J., Yuliarto, B., Kang, Y., Bando, Y., Sugahara, Y. & Yamauchi, Y. (2019). Chemical Design of Palladium-Based Nanoarchitectures for Catalytic Applications. Small, 15 (6), 1804378-1-1804378-27.

Authors
Muhammad Iqbal, Yusuf Valentino Kaneti, Jeonghun Kim, Brian Yuliarto, Yong-Mook Kang, Yoshio Bando, Yoshiyuki Sugahara, and Yusuke Yamauchi

DOI: 10.1002/ ((please add manuscript number))
Article type: Review

Chemical Design of Palladium-Based Nanoarchitectures for Catalytic Applications

Muhammad Iqbal,[1] Yusuf Valentino Kaneti,*[1] Jeonghun Kim,[2,3] Brian Yuliarto,[4] Yong-Mook Kang,[5] Yoshio Bando,[1] Yoshiyuki Sugahara,[6,7] and Yusuke Yamauchi*[2,3,8]

[1] M. Iqbal, Dr. Y. V. Kaneti, Prof. Y. Bando
International Research Center for Materials Nanoarchitectonics (WPI-MANA),
National Institute for Materials Science (NIMS)
1-1 Namiki, Tsukuba, Ibaraki 305-0044, Japan
E-mail: KANETI.Valentino@nims.go.jp

[2] Dr. J. Kim, Prof. Y. Yamauchi
Key Laboratory of Eco-chemical Engineering
College of Chemistry and Molecular Engineering
Qingdao University of Science and Technology, Qingdao 266042, China

[3] Dr. J. Kim, Prof. Y. Yamauchi
School of Chemical Engineering and Australian Institute for Bioengineering and Nanotechnology
The University of Queensland, Brisbane, QLD 4072, Australia
E-mail: y.yamauchi@uq.edu.au

[4] Prof. B. Yuliarto
Department of Engineering Physics and Research Center for Nanoscience and Nanotechnology
Institute of Technology Bandung, Ganesha 10, Bandung 40132, Indonesia

[5] Prof. Y. Kang
Department of Energy and Materials Engineering
Dongguk University-Seoul, Seoul 04620, South Korea

[6] Prof. Y. Bando
Institute of Molecular Plus, Tianjin University. No. 11 Building, No. 92 Weijin Road, Nankai District, Tianjin, 300072, P. R. China

[7] Prof. Y. Bando
Australian Institute of Innovative Materials, University of Wollongong, Squires Way, North Wollongong, NSW 2500, Australia

[8] Prof. Y. Sugahara
Faculty of Science and Engineering
Waseda University, 3-4-1 Okubo, Shinjuku, Tokyo 169-8555, Japan

[9] Prof. Y. Sugahara
Kagami Memorial Laboratory for Materials Science and Technology
Waseda University, 2-8-26 Nishiwaseda, Shinjuku, Tokyo 169-0051, Japan

[10] Prof. Y. Yamauchi
Department of Plant & Environmental New Resources

Kyung Hee University
1732 Deogyeong-daero, Giheunggu, Yongin-si, Gyeonggi-do 446-701, South Korea

Keywords: alloys, catalysis, electrochemical deposition, intermetallic structures, palladium nanoarchitectures

Abstract

Palladium (Pd) plays an important role in numerous catalytic reactions, such as methanol and ethanol oxidation, oxygen reduction, hydrogenation, coupling reactions and carbon monoxide oxidation. Creating Pd-based nanoarchitectures with increased active surface sites, higher density of low-coordinated atoms and maximized surface coverage for the reactants is important. To address the limitations of pure Pd, various Pd-based nanoarchitectures, including alloys, intermetallics and supported Pd nanomaterials have been fabricated by combining Pd with other elements with similar or higher catalytic activity for many catalytic reactions. Herein, the recent advances on the preparation of Pd-based nanoarchitectures through solution-phase chemical reduction and electrochemical deposition methods are summarized. Finally, the trend and future outlook on the development of Pd nanocatalysts toward practical catalytic applications are discussed.

1. Introduction

Noble metals (*e.g.,* Pt, Pd, Ag, and Au) play significant roles in many catalytic reactions, including organic catalysis and electrocatalysis. Among noble metals, Pd is well-known to be highly active for various surface reactions, such as electrocatalysis of hydrogen oxidation, oxidation of small organic molecules, oxygen reduction, hydrogenation, coupling reactions and carbon monoxide oxidation.[1-9] Pd shows a remarkable activity toward the dissociation of hydrogen gas as well as small organic molecules (such as ethanol, methanol, formic acid, *etc.*). Furthermore, Pd is also capable of catalyzing the reduction reaction of oxygen with the presence of electrons and protons. In addition, Pd is known for its high selectivity for some heterogeneous (*e.g.,* the hydrogenation of acetylene) and homogeneous catalytic reactions (*e.g.,* Suzuki reaction, Sonogashira reaction, *etc.*). The high catalytic performance of Pd for these reactions renders them highly promising for many applications, such as fuel cells, pharmaceutical, automotive (catalytic converters) and electrochemical sensors.[6,10-18] In recent years, Pd has gained increasing attention as a substitute for Pt in many electrocatalytic applications. This is because Pd and Pt possess a number of similarities, for example, they belong to the same group in the periodic table and they both exhibit face-centered cubic (*fcc*) structures. Although the economical price of Pd has risen in the last three years due to the high demand from automotive industries (catalytic converters),[18] Pd remains as a promising substitute for Pt in electrocatalysis as it is fifty times more abundant on earth than Pt.[19-21]

The nature of catalytic reactions catalyzed by Pd atoms involves a good understanding of the underlying chemistry at a molecular level. For this purpose, various techniques (such as Auger electron spectroscopy, low-energy electron diffraction, mass spectrometry and thermal desorption spectrometry) have been employed to characterize the surface chemistry of Pd.[22] Pd has three low Miller-index surfaces, *i.e.,* (111), (100) and (110). The Pd(111) surface is a preferential site for CO adsorption, as proven by theoretical and experimental approaches.[23,24] In fact, Pd is the preferred catalyst for the oxidation of hydrogen or liquid fuels, rather than the reduction of oxygen.[26] However, CO is often found as an intermediate product during the electrochemical oxidation of hydrogen and liquid fuels and similar to Pt, Pd is also sensitive to CO poisoning.[26,27]

Proper control over the shape and size of Pd nanoparticles can enable effective tuning of their properties and characteristics for the desired applications.[28-30] The size of the catalyst particles essentially determines the specific surface-active area.[31] The smaller the size of the particles, the larger the specific surface-active area and *vice versa*. The catalytic performance of an electrooxidation catalyst is proportional

to its specific surface-active area. In the early development stage of Pd-based electrocatalysts, many scientists focused on the preparation of the smallest yet optimum size of Pd nanoparticles. However, to further enhance the stability of electrocatalysts upon chemical and mechanical deformations, recent studies have been aimed at controlling not only the size, but also the morphology of Pd by creating various nanostructures from 0D to 3D and exposing the active facets.[32-36]

To date, many groups have reported the preparation of various Pd polyhedrons with specifically exposed facets: cubes with {100} facets, rhombic dodecahedron with {110} facets, and octahedron with {111} facets (**Figure 1**).[37] For instance, Hoshi *et al.* carefully investigated the shape effect of Pd single crystal with different surface structure toward methanol oxidation reaction (MOR).[38] Their experiments revealed that the Pd(111) surface showed the lowest activity, while the Pd(100) surface showed the highest activity for MOR. Furthermore, the Pd(100) surface also exhibited the highest activity toward the formic acid oxidation reaction (FAOR) compared to the other low-index planes.[2] From a theoretical point of view, Wang and co-workers demonstrated for the first time that the activity and selectivity of Pd for the ethanol oxidation reaction (EOR) were highly structure-dependent and that the Pd(100) surface was best at promoting the dissociation of an ethanol molecule with a rather low energy barrier.[39] Furthermore, their DFT study also showed that complete ethanol oxidation could be achieved on the active Pd (100) surface in the presence of hydroxil (OH) group.

Even though the control over the morphology of Pd nanocrystals with low-index planes has been widely explored, recent studies have expanded into the fabrication of 0D, 1D, 2D and 3D Pd nanoarchitectures enclosed with high-index facets.[40,41] In the case of electrooxidation of small organic molecules, catalyst particles with rough surface are preferred. This is because the rough surface of the particles can be translated as having high-index facets, which improve the density of low-coordinated atoms, such as steps, terraces, and kinks.[42] The schematic illustration of low-coordinated atoms is given in **Figure 2**.[43] The presence of a high density of low-coordinated atoms is beneficial for enhancing the amount of active sites available for surface catalytic reactions. Noble metal nanoparticles enclosed with high-index facets have been shown to exhibit better stability and possess a higher density of dangling bonds on the surface, which are preferential for catalysis.[44]

In addition to high activity, the design of highly stable Pd-based nanoarchitectures is also of significant interest. A good catalyst should possess excellent chemical, thermal and mechanical stabilities during the catalytic reactions. Therefore, some strategies have been developed to enhance the stability of Pd-

based nanoarchitectures. The functionalization of Pd by forming alloys or intermetallics with non-noble metals or by dispersing it on support materials is often necessary to improve the stability of Pd. For example, the introduction of a secondary metal (*e.g.,* Au, Ir, Cu, *etc.*) at a certain concentration to form alloys or intermetallics can improve not only the activity but also the chemical stability of the Pd-based catalysts through ensemble and electronic effects.[45-47] The improvement of thermal and mechanical stabilities can be achieved through the fabrication of Pd-based nanoarchitectures with higher dimensions (1D, 2D and 3D), since they have lower vulnerability to dissolution, the Ostwald ripening and aggregation during the reactions compared to 0D nanoparticles.[41,48,49] Apart from alloying, the incorporation of Pd-based nanoarchitectures into support materials, such as carbon and oxides, have also been utilized as a lucrative strategy to enhance their chemical, thermal and mechanical stabilities.[50]

Although Pd-based nanomaterials have been reviewed to some extent in past literatures, these reviews mostly focused on their functional applications, whereas comprehensive reviews on the solution-phase preparation of Pd nanoarchitectures are still limited. As of now, several synthetic strategies have been developed to create a wide variety of Pd-based nanoarchitectures for catalytic applications. This review will focus on the fabrication of various Pd-based nanoarchitectures through chemical reduction and electrochemical deposition methods due to their simplicity and cost-effectiveness.[32,51,52]

The fundamental concepts of this review are illustrated in **Figure 3**. This review is divided into several sections. The first section deals with the nanoarchitectures of Pd catalysts with zero-dimensional to two-dimensional structures, including discussions on the shape and size effects toward some catalytic applications. The second section focuses on the creation of various 3D Pd-based nanoarchitectures, such as aerogels, dendritic and mesoporous structures. The third section explores the functionalization of Pd nanocatalysts (intermetallic, alloys and hybrid structures). Finally, the last section discusses some future directions and challenges related to the fabrication of Pd-based nanoarchitectures toward the development of high-performance electrocatalysts.

2. 0D to 2D Pd Nanoarchitectures

In this section, various types of Pd nanostructures from zero-dimensional (0D) to two-dimensional (2D) nanoarchitectures are discussed. Basically, the 0D morphology refers to unsupported Pd nanoparticles with sizes less than 100 nm on each axis. Meanwhile, 1D morphology refers to Pd particles in which one axis dimension has a size greater than 100 nm (*e.g.*, nanowires, nanotubes, and nanorods). Pd nanoplates, nanosheets, and nanodiscs are classified as 2D Pd nanoarchitectures. The preparation procedures of each kind of morphology and their corresponding properties toward some catalytic applications are discussed.

2.1. 0D – Nanoparticles

The rational design of Pd nanoparticles with exposed facets has been well-reported in the literatures.[53] The synthesis of unsupported colloidal 0D Pd nanoparticles is typically done through seed-mediated or direct (seedless) synthesis. The seed-mediated approach generally consists of two steps: the preparation of small Pd nanocubes as seeds, followed by the growth of polyhedral Pd nanoparticles *via* thermodynamically or kinetically-controlled reactions.[54] The synthesis of Pd seeds typically involves the reduction or decomposition of the Pd metal precursor, followed by nucleation and growth of a single-crystal structure with a particular facet. Directive seed nucleation is commonly assisted by the presence of bromide ions (Br^-) in the reaction solution. For example, in a typical synthesis, Pd precursor (H_2PdCl_4) aqueous solution is added into the CTAB solution and heated at 95 ^oC under stirring. Then, the reduction of the Pd precursor into Pd(0) is achieved with the use of a mild reducing acid, such as ascorbic acid. This reaction then yields cubic Pd seeds which can be used to grow polyhedral Pd particles.[54] To control the growth of the cubic Pd seeds into the desired polyhedron structure, some key factors should be taken into consideration. Niu *et al.* suggested that there were three factors which governed spontaneous nucleation: 1) the amount of seeds added to the growth solution; 2) the reaction temperature and 3) the presence of halide ions (KI) in the growth solution. In particular, adsorbates, such as surfactants or halide anions are often used to alter the surface energy by selectively interacting with different metal crystal facets during the reaction.[55] The strong binding of halides on metallic Pd surfaces suggests that halides could potentially play an important role in the chemical synthesis of Pd nanocrystals by changing the surface energy of different Pd facets, which led to the formation of different final morphology of the Pd nanocrystals. For instance, the presence of Br^- during the synthesis of Pd nanocrystals reported by Xia *et al.* led to the formation of Pd nanocubes and nanobars

enclosed by {100} facets, while in the absence of Br^-, only Pd cubocathedrals enclosed by a mixture of {111} and {100} facets were obtained.[56]

The fabrication of well-defined Pd nanocrystals with various exposed facets can also be achieved by direct (seedless) approaches. Unlike seed-mediated methods, the seedless methods require fewer steps and are easier to perform. For instance, Liu *et al.* employed a halide additive (KBr) to control the shape of Pd nanoparticles from cubic to octahedra (**Figure 4**).[57] Another direct approach to synthesize shape-controlled Pd nanocrystals was demonstrated by Zhang and co-workers through oxidative etching with hydrochloric acid (HCl).[58] They demonstrated that the concentration of HCl added to the reaction solution was crucial for controlling the morphology of the resulting Pd nanocrystals (**Figure 5**). In their report, Pd nanocubes were obtained in the absence of HCl due to the fast reduction rate. However, with the addition of a small quantity of HCl to the precursor solution, truncated nanocubes were formed instead. In contrast, the excessive addition of HCl slowed down the reaction rate even further, leading to the formation of Pd cuboctahedrons. The obtained Pd nanocrystals with three different morphologies were utilized as catalysts for formic acid oxidation. The results revealed that Pd nanocubes with {100} exposed facets showed the best catalytic activity, which was in good agreement with a previous report.[59]

Pd nanoparticles with high-index facets (HIFs) have also been reported in past literatures, including concave nanocubes[60], concave disdyakis triacontahedra[61], concave tetrahedra[62], concave nanocubes[63] and arrow-headed tripods.[64] Pd concave nanocubes enclosed by {730} facets were previously synthesized by Xie *et al.* through a one-pot liquid method. According to their report, Pd nanoarchitectures with various high-index facets could be synthesized by tuning the reaction kinetics, such as temperature and concentration of reducing agent and capping agent.[60,65] At high reaction temperatures (75-80 ^oC), Pd nanocubes were obtained. On the contrary, at lower reaction temperatures and high concentrations of the reducing agent (ascorbic acid), well-defined Pd concave nanocubes were achieved. The obtained Pd nanocubes and concave nanocubes were employed as catalysts toward MOR. It was shown that Pd nanocubes with exposed {100} facets exhibited the best catalytic activity for electrooxidation of alcohols or formic acid compared to other low-Miller index Pd nanocrystals. However, Pd nanocrystals enclosed with HIFs (concave nanocubes) displayed a significantly higher catalytic activity toward MOR by about 2.8 and 50 times compared to Pd nanocubes and commercial Pd/C, respectively.

Well-defined concave tetrahedra Pd nanocrystals were previously obtained through a simple solvothermal process with a high yield. Zhang and co-workers used polyvinylpyrrolidone (PVP) as a

surfactant and both iron(II) acetylacetonate ($Fe(acac)_2$) and ascorbic acid as shape-directing agents.[62] The palladium precursor ($Pd(acac)_2$) and all the other reagents were dissolved in *N*, *N*-dimethylformamide (DMF), which also served as a reducing agent. Following solvothermal reaction at 120 ^oC for 10 h and consecutive washing, concave tetrahedra Pd nanocrystals were obtained. Interestingly, the concave tetrahedra Pd nanocrystals exhibited 3 times higher activity than commercial PdB for formic acid oxidation.

Concave disdyakis triacontahedra Pd nanocrystals (C-DTH Pd NCs) enclosed with {631} facets were prepared through electrochemical deposition on a working electrode from a deep eutectic solvent (DES).[61] The time-dependent experiments revealed that the unique C-DTH structure was evolved from octahedral and icosahedral structures (**Figure 6**). The adsorbed urea in the solvent at the upper limit potential (E_U) of the square-wave potential applied during the electrochemical deposition played a crucial role in the formation of C-DTH Pd NCs. When tested for electrooxidation of ethanol, the C-DTH Pd NCs exhibited a superior specific activity than the Pd nanocrystals with mixed octahedron and icosahedron structures. The high activity of C-DTH Pd NCs was attributed to the presence of high-index facets with high density of low-coordinated atoms, steps and kinks. Controlling the shape of nanoparticles can lead to a change in their molecule-sorption energies, and hence, their catalytic performance. This change typically arises from the modified *d*-band center of a metal nanoparticle as a result of a lattice strain.[66] A lattice strain is typically introduced by crystal twinning during the synthesis of metal nanoparticles, and this can lead to various distinct morphologies, such as decahedra and icosahedra.

2.2. 1D – Nanorods, Nanotubes, Nanowires

1D nanostructures possess several advantages for catalytic applications, due to the enhanced electron and mass transport and improved chemical stability compared to 0D nanoparticles.[48,67-69] Previously, Xu *et al.* reported the fabrication of a highly ordered array of Pd nanowires *via* electrochemical deposition.[70] The array deposition was carried out on the glassy carbon electrode (GCE) assisted by the anodized aluminum oxide (AAO) template. The deposited Pd nanowire array was well-isolated, standing vertically toward the electrode surface, and had a uniform diameter (*ca.* 80 nm) and length (*ca.* 800 nm). When tested for EOR, the Pd nanowire array showed both enhanced activity and stability compared to PtRu/C. It is worth noting that upon increasing the length of the nanowires (6 μm), the mass activity was significantly reduced. This was attributed to the increased diffusion resistance of reactants and products to and from the Pd nanowire array electrode. In contrast to the work by Xu *et al.*, Wang and co-workers successfully prepared ultrathin

Pd nanowires through a polyol method.[71] In the initial growth stage of the nanowires, Pd nanoparticles with diameters of around 2-3 nm were created. To obtain such ultrathin nanowires, a proper control of the reaction kinetics during this initial stage was critical for ensuring the formation of small and thermodynamically unstable nanoparticles and then, the nanowires v*ia* the attachment growth (**Figure 7**). Although the Pd/C particles and ultrathin Pd nanowires have nearly similar geometrical size (2 nm in width for ultrathin Pd nanowires and 2-3 nm in diameter for Pd/C), the ultrathin Pd nanowires displayed 2.5 times higher catalytic activity than the commercial Pd/C catalyst for electrooxidation of formic acid due to the unique wire-like structure and abundance of twin defects.

The synthesis of 1D Pd nanorods with exposed {110} facets *via* an electrochemical deposition has previously been reported by Xiao and co-workers.[72] When employed as an oxygen reduction reaction (ORR) catalyst, these Pd nanorods were as catalytically active as bulk Pt. The superior ORR activity of these Pd nanorods was contributed by the exposed {110} facets, as also indicated by their theoretical study (DFT calculations), in which the O adatom was shown to weakly interact with Pd(110). The morphology-controlled growth of such nanorods was governed by the presence of appropriate halide ions, concentration of Pd precursors, and applied deposition potentials. In this case, the anisotropic growth of the Pd crystal during the synthesis process occurred due to the fast reduction rate. Das group has also reported the synthesis Pd nanorods with an average rod length of 150 nm *via* electrochemical deposition in the presence of nicotinamide adenine dinucleotide (NAD^+) as a shape regulating agent.[73] The selection of appropriate applied pulse width during the electrochemical deposition and concentration Pd precursors in the electrolyte solution were important for ensuring the formation of the nanorods. These Pd nanorods were demonstrated to be highly sensitive and selective for hydrazine detection with low detection limit (LDL) of 5 nM, high sensitivity of 0.78 ± 0.02 μA mM^{-1} cm^{-2} and stable response without any interference from potential interferents, such as Na^+, K^+, NO^{2-}, BrO^{3-}, or Pb^{2+} ions.

As highlighted in this section, 1D Pd nanoarchitectures possess good electronic conductivity. Aside from their intrinsic capability to oxidize several biological substances molecules, such as glucose, lactic acid, *etc*., these 1D Pd nanostructures have also shown excellent performance as non-enzymatic biosensors.[74] For instance, Wang *et al.* had examined porous Pd nanotubes synthesized through an *in situ* galvanic replacement reaction on glassy carbon electrode (GCE) for non-enzymatic glucose sensing.[75] In this work, Cu nanowires were used as a template, however after the galvanic replacement reaction, only pure Pd (no CuPd alloy) was detected in the product, indicating the complete removal of the template. Using an

amperommetric technique, the Pd nanowire sensor was found to generate a wide linear response range from 5 μM to 10 mM for non-enzymatic glucose sensing, with a maximum sensitivity of 6.58 μA mM^{-1} cm^{-2} and a detection limit of 1 μM.

2.3. 2D – Nanoplates, Nanosheets

In recent years, 2D metal nanostructures have attracted increasing attention for catalytic applications.[49,76] This is because they possess abundant low-coordinated atoms at the perimeters, which provide many active sites for enhancing the catalytic activity. To date, several groups have successfully synthesized 2D Pd nanostructures with various distinct structures, such as nanoplates[77-79] and nanosheets[23,80-90]. For example, 2D Pd nanoplates were previously fabricated using two different methods: templated self-assembly and template-free electrochemical deposition methods. Nadagouda *et al.* employed vitamin B_1 as a capping agent for the synthesis of Pd nanoplates, motivated by the use of green chemistry.[77] Apart from its capping properties, vitamin B_1 (reduction potential 0.4 V *vs.* Ag/AgCl) was also considered to be suitable for the reduction of Pd (0.915 V *vs.* SCE). Upon the appropriate selection of solvent and Pd precursor concentration, Pd nanoplates were successfully grown on a single nanorod backbone, generating a leaf-like structure with an average length of several microns. The resulting Pd nanoplates were utilized as effective catalysts for carbon-carbon cross-coupling reactions, such as Suzuki, Heck, and Sonogashira reactions.

On the other hand, Jia group have successfully prepared Pd nanoplate array using an electrochemical route in the absence of any template.[78] The Pd nanoplate array was electrodeposited on a gold substrate by employing a constant potential or current. The key factors which determined the successful growth of these Pd nanoplates were the applied potential and the amount of the surfactant, cetyltrimethylammonium bromide (CTAB).. According to their report, the CTAB used in the electrolyte solution could influence the anisotropic growth of the Pd nanocrystals due its selective adsorption. Hence, with the assistance of uniform electric field between the working and counter electrodes, the initially deposited nanoparticles were able to grow into Pd nanoplates. Furthermore, the obtained Pd nanoplates were found to be superior compared to the flat Pd film electrode for MOR with several times higher catalytic activity. The roughness of the Pd nanoplates was suggested to greatly contribute toward their high surface-active area and consequently, their high catalytic activity for MOR.

Compared to nanoplates, nanosheets are expected to possess higher specific surface area per mass due to their smaller thickness. Therefore, many research groups have reported the successful preparation of

ultrathin Pd nanosheets. For example, Zhang and co-workers reported the controllable synthesis of Pd nanocrystals with various structures ranging from tetrahedral, concave tetrahedral to 2D nanosheets through a direct wet-chemical method.[62] This innovative approach did not require the use of any toxic and/or explosive compounds, such as carbon monoxide or metal carbonyls to assist with the formation of the nanosheets. The fabricated Pd nanosheets had an average length of 124 nm and thickness of 2.3 nm (**Figure 8a**). Their additional experiments revealed that several key factors governed the formation of these nanosheets, including the H_2O/DMF ratio and the strength of the reducing agent (mild reducing agents, such as ascorbic acid were preferred compared to very strong ones, such as citric acid due to their weaker effect on the nucleation of the nanosheets) and the presence of $Fe(acac)_2$ in the reaction solution. Formic acid electrooxidation and catalytic hydrogenation of styrene were selected as model reactions to showcase the excellent catalytic performance of these Pd nanosheets. From the electrooxidation tests, these Pd nanosheets were found to exhibit 3.5 times higher mass activity than the commercial PdB. Furthermore, even after 200 sweeping CV cycles, the mass activity remained as high as 54% of the initial catalytic activity. In addition, these Pd nanosheets also displayed superior performance toward the hydrogenation of styrene with a high conversion rate of 88%, compared to only 38% for commercial PdB.

Later, Qiu and co-workers synthesized free-standing porous Pd nanosheets through a facile one-pot chemical method.[89] Quite similar to Sial's work,[76] the free-standing porous Pd nanosheets were constructed by the interweaving of long ultrathin nanowires (**Figure 8b**). The interweaving of these nanowires was achieved with the assistance of poly(diallyldimethylammonium chloride) (PDDA) and the obtained Pd nanosheets had a dimension of 2.5 μm in lateral length and 10 nm in thickness (**Figure 8c**). Interestingly, by changing the pH of the reaction solution, the sheet-like morphology was transformed into nanoflowers and nanochains at pH 9-10 and pH 12-13, respectively. Therefore, the electrostatic charge distribution on PDDA, hydrogen-bonding forces, electrostatic repulsion, steric forces, PDDA-PDDA interactions, and binding affinity of PDDA-Pd nanoparticles were affected by the variation in the pH value of the reaction solution. The model formic acid oxidation reaction was carried out to probe the superiority of these 2D Pd nanosheets compared to commercial PdB. As expected, the as-obtained Pd nanosheets exhibited a higher mass activity by almost two-fold compared to commercial PdB. Moreover, they also displayed a high stability upon chronoamperommetry (CA) test for 3000 s and accelerated durability test for 1000 cycles. SEM analysis of these Pd nanosheets after the stability test revealed that they successfully maintained the morphology without noticeable changes. In contrast, the commercial PdB particles suffered from severe

aggregation after the stability test. The above examples clearly demonstrate the superiority of 2D Pd nanoarchitectures for such electrocatalytic reactions due to: (1) their lower vulnerability to dissolution, the Ostwald ripening and aggregation during the reactions compared to Pd nanoparticles and (2) their high densities of coordinatively unsaturated atoms and (3) the high active surface area.[49]

3. 3D Pd Nanoarchitectures

In this section, the synthetic methods for the preparation of 3D Pd nanoarchitectures (aerogels, dendritic and mesoporous) are discussed. Pd aerogels are typically comprised of self-supported metallic backbone nanonetworks. The nanonetworks generally consist of a high density of (111) and (100) crystal facets. The interconnected nanonetwork allows Pd aerogels to have a large specific surface area, excellent conductivity, and hierarchical porosity.[91-93] In comparison, the dendritic structure typically shows a branched structure resembling a tree. This unique structure typically possesses large surface area, high mass transport and high density of low-coordinated atoms at their dendritic branches.[94] Furthermore, mesoporous Pd particles typically possess 3D structure (mostly spherical) with highly-ordered pores and pore size ranging from 2 to 50 nm.[95,96] In addition, for certain applications, such as micro fuel cells, mesoporous films constructed by metallic frameworks are generally preferred.[97] In such fuel cells, the catalyst film (porous Pd films) and the current collector (gold layer substrate) are embedded together to form the anode. Moreover, mesoporous films with metallic framework structures are also highly desirable for non-enzymatic electrochemical sensing of specific biomolecules (*e.g.*, glucose, dopamine, lactic acid, *etc*.) with high sensitivity and selectivity.[98]

3.1. Aerogels

Analogous to carbon aerogels, metal aerogels possess both high electrical conductivity and high surface area.[99] Furthermore, due to their intrinsically high catalytic activity, noble metal aerogels are desirable for many electrochemical applications.[100,101] Generally, the preparation of metal aerogels can be achieved through two different strategies (**Figure 9a**), nonetheless both strategies require the formation of a hydrogel. To obtain the hydrogel, the first step involves the gelation of pre-formed noble metal nanoparticles. Next, the hydrogel is spontaneously formed from the metal ions *via* an *in-situ* gelation process.[93] For example, Wen and co-workers reported the controlled growth of porous Pd aerogels through a facile assembly induced by calcium ions (Ca^{2+}) (**Figure 9**).[102] In their report, Ca^{2+} ions were employed as a destabilizing

agent for the preparation of Pd aerogels. Prior to the addition of Ca^{2+} ions, the Pd precursors were reduced with sodium borohydride ($NaBH_4$) in hot water and capped with citrate ions. Here, citrate ions were used to impart electrostatic and steric repulsions to the metal nanoparticles. The addition of Ca^{2+} ions to the concentrated citrate-coated Pd nanoparticles then induced the formation of hydrogels. The aerogels were then formed after subjecting the hydrogels to supercritical drying. According to their report, the concentration of Ca^{2+} could control the volume (porosity) of the hydrogels. The Pd aerogels prepared using higher Ca^{2+} concentration were much denser and exhibited numerous mesopores. When tested for glucose oxidation in the range of 2 to 20 mM, the Pd aerogels with large pore size displayed a high sensitivity of 1.11 μA mM^{-1}, which was 125 and 3 times higher than those of GCE and Pd NPs, respectively.

Later, Burpo *et al.* prepared Pd aerogels through a direct solution-based reduction by employing several combinations of Pd precursors (Na_2PdCl_4 and $Pd(NH_3)_4Cl_2$) and reducing agents (sodium borohydride/$NaBH_4$, dimethylamine borane/DMAB, and sodium hypophosphite/$NaHPO_2$).[103] From their screening, the combination which provided the best aerogel was Na_2PdCl_4 (concentration threshold of 5 mM) and $NaBH_4$ (0.1 M). The effectiveness of reducing agents in terms of forming aerogel was in the order of $NaBH_4$ > DMAB > $NaHPO_2$. The well-formed Pd aerogels had an average ligament diameter of 34.5 ± 9.5 nm and an average pore size of 82.7 ± 57.7 nm (**Figure 9c**). More recently, Yazdan-Abad and Douk group successfully prepared Pd aerogels with electrochemical surface-active area as high as 56.1 and 133.3 m^2 g^{-1}, respectively.[104,105] Moreover, their mass activity toward the electrooxidation of ethanol was 6-7 times higher than that of commercial Pd/C. The superior catalytic performance of these Pd aerogels was attributed to their hierarchical porosity (macropores and mesopores), improved structural stability and enhanced transport of electrons. Here, the mesopores could provide more active sites and high surface-active area, while the macropores could ensure easier access for reactants to the active sites. The above examples clearly highlight the benefits of Pd aerogels for electrocatalytic applications.

3.2. Dendritic Structure

By nature, most metals, such as Ni, Pd, Pt, Cu, Ag and Au have a *fcc* crystal structure. As such, to form 3D dendritic structure from these metals, surfactants are usually required as shape-directing agents by preferentially adsorbing on specific crystal planes. Zhou *et al.* proposed the formation of Pd dendrites *via* a polyglycol-assisted oriented attachment process.[106] The polyglycol played a crucial role as a structure-directing agent by promoting the structural evolution of small urchin-like particles formed during the initial

growth stage into dendrite-like particles. In addition, hydrazine hydrate ($N_2H_4.H_2O$) and ammonia (NH_3) were also utilized to reduce the Pd precursor ($PdCl_2$) and to regulate the pH value of the reaction solution, respectively.

Patra and co-workers previously synthesized Pd dendrites with a high density of surface steps by controlling the growth along the (110) direction.[107] In their work, the electrodeposition method (using AC impedance technique) was used to deposit branched Pd dendrites on the carbon paper electrode. The growth of these dendrites was greatly contributed by the instabilities induced by sinusoidal potential applied during the electrodeposition process, as such dendrites were not observed when DC potential was applied under similar conditions. The presence of many surface steps on these dendrites greatly contributed toward their enhanced activity for the formic acid oxidation. It is believed that the high step density provided many active sites for the adsorption of formic acid molecules. In other report, Pd dendrites had also been grown on carbon fiber cloth *via* electrochemical deposition with potential pulse technique in the presence of perchloric acid.[108] Moreover, Zhao and co-workers have also successfully synthesized Pd dendrites from the electrolyte solution (containing Pd precursor and hydrochloric acid) using electrodeposition technique.[109] It is worth noting that in both reports, acids were used to increase the ionic conductivity of the electrolyte solution as high ionic conductivity was essential for ensuring good transport of ions from the electrolyte to the working electrode.[110]

More recently, Bai and co-workers prepared dendritic Pd nanoparticles through a facile chemical reduction process.[111] In their synthesis, CTAB was used as a shape-directing agent and ascorbic acid was used as a mild reducing agent. Interestingly, the presence of a small amount of nickel ions (Ni^{2+}) was necessary to ensure the formation of these Pd dendrites, although their exact role is still unclear. A spectroscopy study (*i.e.*, X-ray photoelectron spectroscopy or XPS study) on the electronic coordination state of dendritic Pd nanoparticles revealed that the binding energies of Pd^0 and $Pd^{II}O$ were negatively shifted by *ca*. 0.86 eV compared to those of commercial Pd catalyst.[112] This implies that the dendritic morphology affected the electronic structure of Pd, leading to better electrocatalytic activity, enhanced stability and superior CO tolerance compared to the commercial Pd catalyst.

3.3. Mesoporous Pd Particles and Films

In general, the fabrication of well-ordered mesoporous metals can be performed through two main methods: hard-templating and soft-templating methods.[113-118] In the hard-templating method, mesoporous silica or

mesoporous carbon is commonly used as a hard template. Generally, the hard-templating method involves multiple steps: (1) the preparation of the template; (2) the deposition of metallic materials on the template and (3) the removal of the template (**Figure 10a**).[118] For instance, Ye *et al.* previously reported the preparation of 3D ordered mesoporous (3DOM) Pd network templated by silica super crystal.[120] The silica nanoparticles were self-assembled into super crystal by centrifugation. Then, the silica super crystal was impregnated with metal ions by adding the dried silica super crystal into the Pd precursor solution and hydrazine was used to reduce the Pd salt to metallic Pd. In the final step, the siliceous template was removed by dissolution in hydrofluoric acid (HF). The 3DOM Pd network replicated from the silica template exhibited pore wall thickness of *ca.* 3-8 nm and pore diameter of *ca.* 40 nm (**Figure 10b**). In their report, several parameters, such as the concentration of the Pd precursor, the volume ratio of the Pd precursor to the pore size of the silica super crystal template and the reduction rate could influence the formation of the 3DOM Pd network. Since hydrazine could induce fast reduction of Pd, interconnected Pd network was observed. However, the 3DOM Pd network was not observed when the reduction process was carried out using either dimethylamine borane (DMAB) or hydrogen gas (H_2). When tested as an electrocatalyst for formic acid oxidation, the 3DOM Pd network displayed both higher electroactivity and better electrochemical stability than commercial PdB.

Pd nanoarrays with hexagonally-closed mesoporous structures were previously fabricated using SBA-15 as a template (**Figure 10c**).[120] These nanoarrays exhibited an average pore size of *ca.* 3.2 nm and a moderate surface area of 29.5 m^2 g^{-1}. It is worth noting that the use of different template will lead to different arrangement of the mesoporous Pd structure. SBA-15-templated mesoporous Pd structure typically consists of hexagonally-arranged cylindrical Pd nanowires (the exact inverse replica of SBA-15) interconnected by self-supported shorter wires. This is because of the occupation of Pd in the channel-interconnecting micropores within the SBA-15 wall.[121,122] The mesoporous silica KIT-6 has also been employed as a hard template for the synthesis of mesoporous Pd networks, as reported by Wang *et al.* (**Figure 11**).[123] The catalytic properties of these mesoporous Pd networks varied with the different topology in the enantioselective hydrogenation of acetophenone and its derivatives. The enantioselectivity over the mesoporous Pd catalysts increased in the sequence of double gyroid structure (*Ia*3*d*) > single gyroid structure ($I4_132$) > 2D hexagonal structure (P6mm) > ultrafine Pd black. The double gyroid structure was obtained with the KIT-6 template treated at 130 ^oC and KBH_4 was identified to be the best reducing agent. The double gyroid mesoporous Pd network showed an excellent performance in the enantioselective

hydrogenation test due to the unique spatial arrangement with the optimum pore size. Moreover, the desired lattice structure formed by the KBH_4 reduction provided the appropriate micro-environment for improving the enantio-differentiation. Hence, the enantioselectivity could be tuned by manipulating the confinement effect in the catalyst structure.[124]

The fabrication of mesoporous metals using soft-templating method is typically achieved by lyotropic liquid crystals (LLCs)[125-127] and micelle assembly[128-137]. In the LLC approach, there are several lyotropic phases, including cubic *Ia*3*d*, lamellar, and hexagonal phase. Bartlett and co-workers reported the synthesis of mesoporous Pd layers with a hexagonal pore arrangement using the hexagonal LLC template (**Figure 12a**).[127] The thickness of the metallic layers could be controlled by adjusting the total charge. The obtained mesoporous Pd layer had average pore diameter and pore-to-pore distance of 3 nm and 6 nm, respectively. (**Figure 12b**), with a relatively high electrochemical surface-active area (ECSA) of 39 m^2 g^{-1}. Interestingly, the pores were found to run continuously from the outer surface to the inner pore walls. Thus, by carrying out the deposition in several stages, continuous pore structure could be achieved, leading to the high ECSA.

Compared to LLCs, the utilization of block copolymers as soft templates can enable the attainment of mesoporous Pd with larger pore size. Cappillino *et al.* successfully demonstrated the fabrication of mesoporous Pd with tunable porosity by changing the block size of the block copolymer, poly(styrene-*b*-ethylene oxide) (PS-*b*-PEO).[128] Two block copolymers, PS_{2300}-*b*-PEO_{3100} and PS_{3800}-*b*-PEO_{5000} were utilized as soft templates and the prepared mesoporous Pd particles were denoted as Pd_S and Pd_L, respectively. The formation mechanism of the mesoporous Pd can be described as follows (**Figure 12c**). The block copolymer arranged hexagonal array of cylindrical micelles. The hydrophobic PS block and the hydrophilic PEO block formed the core and shell of the micelles, respectively. The PEO block solvated the metallic ions in aqueous phase. The pores were formed on the regions which were previously occupied by the templates following their removal. In this case, the pore walls or backbones were constructed by metallic Pd. Interestingly, the use of different molecular weight of the block copolymer PS-*b*-PEO generated different average pore size for the resulting mesoporous Pd particles. The average pore sizes of Pd_S and Pd_L were 7 nm and 13 nm, respectively, consistent with the pore sizes observed by TEM (**Figure 12d,e**).

Cationic surfactants, such as cetyltrimethyl ammonium bromide (CTAB), cetyltrimethyl ammonium chloride (CTAC), hexadecylpyridinium chloride (HDPC), cetylpyridinium chloride (CPC) and non-ionic surfactants, such as Pluronic F127 and P123, can assist the formation of mesoporous Pd *via* chemical reduction. For example, Zhang and co-workers successfully prepared spherical mesoporous Pd particles with

an average diameter of *ca.* 33 nm and rough surface by utilizing CTAC as a structure-directing agent (**Figure 13a**).[130] An in-depth structural analysis of an individual sphere by TEM revealed that each sphere was actually composed of smaller nanoparticles with an average size of 7 nm (**Figure 13b**). Later, Li *et al.* reported the successful size-controlled synthesis of spherical mesoporous Pd particles by employing dual surfactants, HDPC and F127 (**Figure 13c, d**).[132] In their report, the reaction solution consisted of HPDC, F127, Na_2PdCl_4 and ascorbic acid, which acted as shape-directing agent, protecting agent, Pd source and reducing agent, respectively. The size of the mesoporous Pd particles could be easily controlled by tuning the amount of F127 in the reaction solution. The rough surface of these particles was caused by the oxidative etching process as a result of the sufficient amount of Cl^- ions derived from the cationic surfactant. When tested for formic acid oxidation, the mesoporous Pd catalyst exhibited more than double the activities of commercial Pd black and Pd nanoparticles, along with better electrochemical stability. The superior activity and stability were attributed to the mesoporous nature of these particles with high-index facets, which provided a high density of active sites. Apart from spherical mesoporous Pd particles, mesoporous Pd film has also been fabricated *via* electrodeposition with the assistance of CTAC.[134] The applied deposition potential was fixed at a constant value to attract metallic ion complexes in the electrolyte solution toward the working electrode and to ensure successful reduction of the metallic ion complexes to the metallic state. Interestingly, the deposited Pd film formed vertical mesochannels with pore channel size of 2.1 ± 0.2 nm and channel wall size of 3.3 ± 0.2 nm (**Figure 14**). The presence of these vertical mesochannels ensured easier access for the reactant and product to and from inner side of the pores, owing to the lower diffusion resistance.[116] Although various surfactants have been successfully utilized as pore-directing agents in the fabrication of mesoporous metals, achieving mesoporous Pd particles with controllable pore size and orientation using surfactants is still challenging and further studies are needed to resolve this issue in the future.

4. Functionalization of Pd-based Nanocatalysts

4.1. Pd-Based Alloys and Intermetallics

Despite its high catalytic activity, pure Pd cannot exceed the performance of Pt in many catalytic reactions. Furthermore, the intermediates produced during the oxidation of small organic molecules, such as carbon monoxide (CO) are often strongly adsorbed on the Pd surface, thereby lowering its catalytic performance. In the case of oxygen oxidation reaction, the oxygenated species tend to adsorb on the surface of pure Pt or Pd

catalyst. In addition, pure Pt or Pd catalysts suffer from poor alcohol tolerance when employed in direct alcohol fuel cells. Therefore, the development of intermetallics or Pd alloys with non-noble metals has gained significant momentum in the last ten years to produce cheaper high-performance catalysts with enhanced stability.[138-147] The tolerance of Pd to poisoning species in direct alcohol fuel cells can be enhanced by combining or alloying it with other transition metals (*e.g.*, Ni, Co, Fe, Cu, Cr, Mo, and W). Such enhancement is believed to have arisen from two possible mechanisms: 1) the neighboring sites of Pd atoms from the second element provide oxygenated species that induce surface reactions with Pd-adsorbed poisoning species and 2) the alloy structure shift the energy of Pd electronic states, thus weakening Pd-poisoning species interaction.[148-154] In the case of electrooxidation of ethanol, incomplete oxidation of ethanol sometimes occurs due to the decreased capability of Pd to break the C−C bond when the ethanol oxidation goes through the C_2 pathway.[155] Therefore, by alloying Pd with other element(s), it becomes possible to completely oxidize ethanol into CO_2.[156-158] Meanwhile, in the case of cathodic catalyst, increased alcohol cross-over tolerance can be achieved by weakening the bond strength of the oxygenated species on the catalyst surface.

To date, numerous Pd-based intermetallics and alloys have been reported in the literatures.[159-188] **Table 1** lists an exhaustive summary of previously reported Pd-based alloys and intermetallics, including their synthetic approach, application and properties. The most common solution-based methods for generating Pd-based alloys or intermetallics are chemical reduction, galvanic replacement reaction and polyol method. With regard to the chemical reduction method, the reduction and deposition of the secondary element on Pd to prepare the bimetallic alloys are typically achieved through underpotential deposition (UPD). For instance, Pd-Cu bimetallic alloys with tripod architectures were previously reported by Zhang and co-workers.[174] To generate such alloys, the Cu atoms were deposited on the Pd surface after the preferential reduction of $PdBr_4^{2+}$ into Pd metal (**Figure 15a**). The Pd ions could be directly reduced to metallic Pd by ascorbic acid. Meanwhile, in the absence of Pd precursors in the reaction solution, no Cu particles were obtained, indicating that the Cu UPD could only occur on the metal surface with a higher redox potential than its standard reduction potential. The formation of the tripod Pd-Cu bimetallic alloys was governed by the presence of Cu precursor and the amount of KBr in the reaction solution. In the absence of Cu precursor, only Pd nanoparticles with cubic morphology were obtained. When a small amount of Cu precursor was introduced in the reaction solution, the cubic Pd nanoparticles were transformed into Pd-Cu alloy with a mixture morphology of cubic and tripods. Upon the addition of more Cu precursor, Pd-Cu tripods with clear

branched arms were observed (**Figure 15b**). In the early stage of the synthesis (t = 10 min), the small plate-like particle seeds of *ca.* 4 nm in size with a triangular shape were formed, together with very short arms. The branched tripod structures grew along three <211> directions as the synthesis process proceeded. The atomic arrangement on the side face of the arm branches was characterized by the alternation of {111} and {100} atom steps (**Figure 15d and 15e**). In addition, the formation of the tripod morphology was also facilitated by the Br^- ions. Here, the growth direction was affected by the strongly bonded Br^- ions to the three of the {100} side faces of a triangular plate, which forced the Pd atoms to grow on the three corners of the plate-like seed to generate the tripod structure (**Figure 15c**). The bimetallic PdCu catalyst was found to exhibit almost 9 times higher mass activity for formic acid oxidation than the commercial PdB along with better stability due to the contribution from the high-index facets.

More recently, Fan *et al.* successfully created ultrathin PdCu nanosheets with average thickness of 2.71 ± 0.48 nm and lateral size of 33.8 ± 8.3 nm through a solvothermal method (**Figure 16a**).[175] In their synthesis, CO molecules and *n*-butylamine were used as capping agents by promoting anisotropic growth. In addition, *n*-butylamine also assisted the reduction of Cu^{2+} by creating complexes between Cu^{2+} and ammonium. In addition, the wrinkle-free nanosheet morphology was also affected by the presence of PVP and CTAB in the reaction solution, which acted as stabilizing agent (to prevent aggregation) and shape-directing agent, respectively. By changing the ratio of the initial Pd and Cu precursors, the final composition of the PdCu alloy could be tuned (**Figure 16c**). Interestingly, these bimetallic nanosheets exhibited modulated electronic structures of Pd atoms, as evidenced by theoretical and experimental observations. The theoretical study by density functional theory (DFT) calculations showed that the *d*-band center of PdCu nanosheets (−2.44 eV) was further away from the Fermi level, as compared to that of PdCu nanoparticles (−2.25 eV). The XPS results also supported the DFT calculations, as indicated by the shift of the core-level XPS peak of Pd in PdCu nanosheets by about 0.25 eV toward higher binding energy relative to that of PdCu nanoparticles, indicating a down-shift of the *d*-band of PdCu nanosheets (**Figure 16b**). These findings suggested that the introduction of Cu atoms could effectively decrease the bonding between the adsorbate and Pd surface which in turn, improved the catalytic activity and stability of the bimetallic PdCu nanosheets.

The intermetallic structure differs from its counterparts (alloy and bimetallic) in terms of its ordered structure which leads to uniform surrounding of the active sites. This allows that the numbers of neighboring sites and the distance between neighboring sites to be easily identified by experimental and theoretical techniques. However, the ordered structure is typically achieved by post-synthetic heating at a very high

temperature (1000 ^{o}C). Previously, two different groups reported the fabrication of intermetallic Pd_3Pb and Pd_2Ge nanonetworks *via* one-pot reduction and solvothermal methods, respectively, at low reaction temperatures (170 ^{o}C and 220 ^{o}C). The ordered Pd_2Ge nanonetwork was firstly reported by Sarkar and co-workers.[159] To synthesize this intermetallic nanonetwork, K_2PdCl_4 and $GeCl_4$ were used as the metal precursors, superhydride ($Li(Et_3BH)$) was employed as the reducing agent and tetraethylene glycol (TEG) was utilized as the solvent. Their TEM analysis revealed that in the initial stage of the reaction, Pd_2Ge was formed as small nanoparticles. Then, after 24 h, the as-formed intermetallic particles grew larger and became joined together (**Figure 17a**). Through further reaction (36 h), the joined particles formed a large connected network (**Figure 17b**) *via* oriented attachment (**Figure 17c**). The covalent bonding strength between Pd and the secondary element in the intermetallic structure was studied by XPS. As seen in **Figure 17d-g**, the binding energies of the core-level Ge peaks were shifted down by 0.7 eV compared to elemental Ge, indicating the existence of a strong covalent bond between Pd and Ge. When tested for EOR, the ordered Pd_2Ge nanonetwork exhibited not only higher activity but also better stability than the commercial Pd/C catalyst. The superior electroactivity of the intermetallic Pd_2Ge nanonetwork was attributed to the perfect balance between the adsorption energies of the reaction intermediate species, such as CH_3CO and OH. Their theoretical simulations revealed that the intermetallic Pd_2Ge could bond strongly to OH, however it was only weakly bonded to CH_3CO.

Ordered Pd_3Pb nanonetwork has previously been prepared by Shi *et al.* through a one-pot reduction method at low temperatures.[160] The metal precursors (Na_2PdCl_4 and $Pb(acac)_2$) were co-reduced by citric acid and the solvent, ethylene glycol. In addition, the anisotropic growth of the nanonetwork was dictated by the capping agent PVP. The XRD pattern of the ordered Pd_3Pb nanonetwork showed the typical five peaks assigned to (111), (200), (220), (311), and (222) along with six additional peaks (so-called "ordering peaks") assigned to (100), (110), (210), (211), (300) and (310) planes of Pd_3Pb *cP*4 crystalline type (space group $Pm\bar{3}m$(221)), thereby confirming the formation of the intermetallic phase. The inter-diffusion of Pb atoms for creating structurally ordered and chemically stable intermetallic phase was important for optimizing the electronic and geometric effects (rough surfaces with abundance of opening channels within the nanonetwork) by downshifting the *d*-band center. This in turn, weakened the adsorption energy of the reaction intermediate products, accelerated the desorption rate and enhanced the catalytic activity, CO tolerance and stability.

Apart from chemical reduction, electrochemical deposition has also been shown to be effective for creating nanoarchitectures of Pd-based alloys. For instance, Tominaka *et al.* reported the fabrication of mesoporous PdCo sponge-like film using electrochemical deposition and de-alloying techniques. The aqueous electrolyte solution consisted of a mixture of $[Pd(NH_3)_4]Cl_2$, NH_4Cl, $CoCl_2$ and malonic acid.[164] Electrochemical deposition of the mesoporous PdCo film was carried out at a constant potential of -0.9 V *vs.* Ag/AgCl for 10 min at 14 ± 2 ^oC. The mesoporous structure was formed through a subsequent electrochemical de-alloying process by applying a potential of 0.6 V in nitrogen-saturated 0.5 M H_2SO_4 for 6 h at room temperature. The determination of the applied deposition potential through linear sweep voltammogram (LSV) of the electrolyte solution consisting more than single metal complexes could not be determined as a simple summation of those individual voltammogram profiles. The linear sweep voltammogram (LSV) profile of the PdCo electrolyte solution showed a unique profile, in which the deposition current increased as the potential was decreased from −0.2 to −0.8 V (**Figure 18a**). Comparison of the LSV profiles of PdCo and Co revealed that the reduction and deposition of Co atoms in PdCo occurred through underpotential co-deposition. The quality of the as-deposited mesoporous PdCo film could be enhanced by de-alloying technique, which further improved the porosity by *ca.* 62%, but also reset the Pd and Co composition ratio to 92:8. Such a high level of porosity was beneficial for ensuring good oxygen diffusion and the Pd:Co composition ratio of 92:8 was reported to be the optimum composition for obtaining the best ORR activity (**Figure 18b-e**). More importantly, the mesoporous PdCo film displayed a higher ORR activity than the typical Pt electrode, owing to their unique geometric features and enhanced electronic properties.

4.2. Supported Pd Nanoparticles

The use of support materials which have larger particle size than the actual catalyst can enable the catalyst particles to be well-dispersed on the support.[189] Good dispersion of the catalyst particles will increase the catalyst contact area with the reactant(s), leading to better catalytic activity, while also reducing the loading of catalyst.[190] To date, numerous materials have been utilized as support materials for noble metal catalysts, including carbons[191-193], oxides[194-196], carbides[197-199] and electroconductive polymers [200-204]. For electrocatalytic applications, some requirements should be fulfilled by the support materials to ensure their successful utilization.[205] These requirements are: (1) high surface area for ensuring good dispersion of metallic catalyst particles; (2) high electrical conductivity; (3) good interaction with the metallic catalyst

particles, either through electrostatic, van der Waals, or covalent bonding and (4) high tolerance to poisoning, corrosion and mechanical deformation.

Strong electronic interaction between the metallic catalyst particles and the support material is crucial for achieving high catalytic activity.[206] Several analytical techniques (XPS and Raman spectroscopy) and DFT calculations can be employed to characterize and predict the interaction and charge transfer distribution at the Pd-support interface.[207] For instance, Rao *et al.* revealed the correlation between support functionalization and charge distribution at the Pd-carbon interface. It was shown that carbon support could modify the electronic properties of Pd and therefore, enhanced the catalytic activity.[208]

Carbon black is commonly employed as a carbonaceous support for electrocatalysts due to their high surface area and electrical conductivity. However, its high surface area is mostly contributed by the large density of micropores (<1 nm), which is not good for the dispersion of the metallic catalyst particles and the flow of the reactant(s). In contrast, ordered mesoporous carbon (OMC) and carbon gels are preferred host materials for the deposition of metallic catalyst particles.[209] Furthermore, emerging graphitic carbon materials (*e.g.*, graphene and carbon nanotubes) have also drawn significant attention as catalyst supports due to their unique structures and properties, which can affect the chemical stability of the catalyst.[210]

Although commercial carbon black-supported Pd catalysts are widely available on the market, recent studies have been aimed at synthesizing small-sized Pd particles on the carbon support with better size uniformity and improved dispersion. For example, Wang *et al.* successfully prepared monodisperse small-sized Pd particles with an average size of *ca.* 3.8 nm on Vulcan XC-72 through a one-pot reduction method at room temperature.[211] The size of these Pd particles was more uniform compared to the commercial Pd/C particles (**Figure 19a** and **19b**). The deposition of the Pd nanoparticles on the carbon surface was achieved through a mild reduction process in the presence of DMF and *N*, *N*-diethylaniline borane (**Figure 19c**). In this process, DMF provided a free pair of electrons which could interact with the carbon surface and promoted the formation of monodisperse Pd atoms/cluster on the carbon support. Furthermore, the use of *N*, *N*-diethylaniline borane enabled alkyl substitution to nitrogen, which could prevent the overgrowth of Pd nanoparticles. The resulting carbon-supported monodisperse Pd catalyst exhibited 2.5 times higher ECSA than the commercial Pd/C particles, as investigated by CO-stripping experiments.[212] Correspondingly, they displayed around 2.6 and 4 times higher mass activity than the commercial Pd/C catalyst toward formic acid and ethanol oxidation, respectively. Pd nanoparticles supported on OMC for electrooxidation catalyst have been reported by Hu *et al.*[213] OMC possesses larger pore size and hence, it can host more Pd nanoparticles

as well as provide more accessible channels for the reactants and products. Pd nanoparticles with an average size of 3 nm were easily decorated on the highly ordered mesoporous structure with an average pore diameter size of 4.7 nm (**Figure 20a-c**). The agglomeration of Pd nanoparticles during self-assembly and growth could be prevented by adding dimethylamine hydrolyzed from DMF as the solvent, as illustrated in **Figure 20d**. A significant fraction of Pd nanoparticles inside the porous structure was observed from the decrease in mean surface area (around 22.4%) of non-decorated OMC and Pd-decorated-OMC through the analysis of nitrogen adsorption isotherms (**Figure 20e and 20f**). Pd-decorated-OMC showed significant improvement in catalytic activity toward both ethanol and methanol oxidation compared to PdB and Pd/C. Hollow graphitic carbon nanocages synthesized using magnesium oxide (MgO) as a sacrificial template have been utilized as support for Pd nanoparticles (*i.e.,* Pd/CN catalyst).[214] Owing to its large surface area, uniform dispersion and excellent electrical conductivity, the Pd/CN catalyst could outperform commercial Pd/C catalyst in EOR.

Emerging carbonaceous materials, such as carbon nanotubes (CNTs), carbon nanofibers (CNFs), graphene and reduced graphene oxide (RGO) have been widely used as support materials for Pd nanoparticles.[215-218] Recently, Mondal and co-workers reported a new approach to unzip single-walled CNTs (SWCNTs) simultaneously with the formation of small-sized Pd nanoparticles encapsulated with a graphitic carbon layer. This approach could ensure the successful integration of the metallic catalyst with the honeycomb carbon network, leading to high electrocatalytic activity toward oxidation of formic acid.[219] There are still some challenges with regard to the deposition of small-sized Pd nanoparticles on the carbon support: (1) How to avoid the agglomeration of Pd nanoparticles; (2) How to prevent the overgrowth of Pd nanoparticles; (3) How to maintain the original carbon structure during growth and/or attachment of Pd and (4) how the Pd nanoparticles can be anchored/attached well on the support surface. A natural polymer, such as deoxyribonucleic acid (DNA), was recently employed to promote the growth of small-sized Pd clusters and to modify the surface of CNTs to prevent aggregation and provide sufficient binding sites.[220] The effect of the size of Pd nanoparticles on the ECSA was studied by Yang *et al.* and Zhang *et al.* Their studies revealed that larger-sized Pd nanoparticles (average size of *ca.* 20 nm) exhibited lower ECSA than smaller-sized ones (average size of *ca*. 4.2 nm).[221] Pd nanoparticles supported on helical carbon nanofibers (Pd/HCNFs) have been reported by two different groups.[222,223] Hu and co-workers utilized a specific type of functional group (phenyl groups) to anchor uniform small-sized Pd nanoparticles (an average size of 4.5 nm) on the surface of hollow carbon nanofibers (HCNFs) through π- π interaction.

Graphene sheets have also been utilized as support for Pd nanoparticles.[224-226] However, their restacking property, aggregation of metal particles on the pristine sheet surface, and insufficient binding sites present major problems for graphene sheets. To solve these problems, chemical functionalization and chemical doping with heteroatoms should be performed prior to attaching Pd nanoparticles on the sheet surface.[227,228] Kiyani *et al.* Have successfully synthesized uniform small-sized Pd nanoparticles with good dispersion on the surface of nitrogen-doped graphene (NG) sheets. The N-doped graphene sheets exhibited many surface defects which provided good deposition sites for metal nanoparticles.[229] The anchoring of Pd nanocatalysts with exposed high-index facets on 2D support materials, such as graphene sheets is still rarely reported. The successful anchoring of Pd nanoparticles with multi-edges and corners on graphene support was previously reported by Liu and co-workers.[230] The preparation of these graphene-supported Pd nanoparticles comprised of three steps: (1) the preparation of graphene oxide (GO) by modified Hummers‘ method followed by the reduction of GO into reduced graphene oxide (RGO); (2) the preparation of Pd nanoparticles and (3) the assembly of Pd nanoparticles on the RGO support. In this work, ascorbic acid was employed as both reducing and structure-directing agents. Interestingly, the incorporation of the Pd nanoparticles on the RGO support did not alter the morphology as well as the uniformity of the Pd nanoparticles. Such incorporation however, has successfully prevented the agglomeration of Pd nanoparticles and improved their dispersion on the RGO surface**.** The covalent bond strength of the Pd nanoparticles and RGO support has been calculated theoretically and according to their report, the Pd adatoms on graphene preferred B-site bonding than T-site or H-site. Multi-edges and corners are expected to provide enhanced charge transfer efficiency as these structures can promote the spontaneous formation of localized electric field. The corresponding mechanism of electron transfer from the corner of the Pd nanoparticles to the RGO occurred through strong covalent interaction between Pd nanoparticles and RGO. In comparison to Pd nanoparticles and commercial Pd/C catalyst, the electrocatalytic performance of the Pd/RGO hybrid was higher. This enhancement was attributed to the novel morphology of the nanoparticles with multi-edges and corners, the enhanced conductivity, and the higher surface area contributed by the RGO.

5. Summary and Outlook

Recent advances on the fabrication of Pd-based nanoarchitectures by solution-phase chemical reduction and electrochemical deposition methods toward the development of cost-effective and high-performance catalysts were reviewed. By designing Pd nanoarchitectures with specifically exposed facets and controlled morphology, Pd nanocatalysts with outstanding catalytic performance for many catalytic reactions can be achieved. Furthermore, by combining Pd with non-noble elements and/or support materials can enhance its catalytic performance and stability toward corrosion and harsh reaction conditions.

Solution-phase methods have been used to prepare a wide variety of Pd nanoarchitectures from 0D to 3D either through seed-mediated or direct (seedless) synthesis. Regardless of the method, halide additives are commonly used to direct the growth of the particles along a certain direction or to etch specific planes. To avoid the risk of dissolution, the Ostwald ripening and aggregation associated with 0D nanoparticles, higher dimensional Pd nanoarchitectures (1D to 3D) are generally preferred. Furthermore, they can provide better electron and mass transport, greater abundance of low-coordinated atoms and hierarchical porous structures, leading to higher catalytic activity. Despite some success, there are still some limitations with respect to the solution-phase synthesis. First, traces of additives and surfactants involved in the reaction should be completely removed from the final product or they will lower the catalytic performance. Post-synthetic cleaning by ozone treatment or high-temperature heating are usually necessary to ensure complete removal of unwanted elements or organic compounds from the product. In the case of supported Pd nanocatalysts, the combination of 2D or 3D Pd nanoarchitectures or hybrids (intermetallics/alloys) with support materials has rarely been reported in the literatures. The synergistic effect of the support material to enhance the charge transfer (and dispersion of the active catalyst) and the abundance of active sites offered by 2D or 3D nanoarchitectures are expected to produce significantly higher performance than supported 0D nanoparticles.

From economical viewpoint, the price of Pd has increased steadily over the past two years. However, the Pd resource on earth is at least fifty times larger than Pt and hence, Pd can still partially be used to reduce the heavy demand for Pt catalyst. The combination of Pd with non-noble elements, such as transition metals, is expected to provide cost-effective catalysts with similar or higher catalytic activity than pure Pt or Pd catalyst. Furthermore, to improve the feasibility of Pd-based catalysts toward real-life catalytic applications, more efforts into development of facile, greener and scalable synthetic methods should be carried out in the future.

Acknowledgements

This work was supported by Australian Research Council (ARC) Future Fellowship (FT150100479). This work was partly supported by the International Energy Joint R&D Program of the Korea Institute of Energy Technology Evaluation and Planning (KETEP), granted financial resource from the Ministry of Trade, Industry and Energy, Republic of Korea (No. 20168510011350). M.I. would like to thank the Indonesia Endowment Fund for Education (LPDP) for the financial support. Y.V.K. thanks the Japan Society for Promotion of Science (JSPS) for providing the standard postdoctoral fellowship.

Received: ((will be filled in by the editorial staff))
Revised: ((will be filled in by the editorial staff))
Published online: ((will be filled in by the editorial staff))

References

[1] Y.-Y. Yang, J. Ren, Q.-X Li, Z.-Y Zhou, S.-G Sun, W.-B. Cai, *ACS Catal.* **2014**, *4*, 798-803.

[2] K. Jiang, H.-X Zhang, S. Zou, W.-B. Cai, *Phys. Chem. Chem. Phys.* **2014**, *16*, 20360-20376.

[3] L. Guczi, Á. Molnár, D. Teschner, in *Comprehensive Inorganic Chemistry II (Second Edition): From Elements to Applications*, Vol. 7 (Eds: J. Reedijk, K. R. Poeppelmeier), Elsevier Ltd., Amsterdam, Netherlands **2013**.

[4] L. Liu, A. Corma, *Chem. Rev.* **2018**, *118*, 4981-5079.

[5] Q.-A. Chen, Z.-S. Ye, Y. Duan, Y.-G. Zhou, *Chem. Soc. Rev.* **2013**, *42*, 497-511.

[6] B. Cai, S. Henning, J. Herranz, T. J. Schmidt, A. Eychmüller, *Adv. Energy Mater.* **2017**, *7*, 1700548.

[7] P. B. Kettler, *Org. Proc. Res. Dev.* **2003**, *7*, 342-354.

[8] E. J. Peterson, A. T. DeLaRiva, S. Lin, R. S. Johnson, H. Guo, J. T. Miller, J. H. Kwak, C. H. F. Peden, B. Kiefer, L. F. Allard, F. H. Ribeiro, A. K. Datye. *Nat. Commun.* **2014**, *5*, 4885.

[9] M. Shao, *J. Power Sources* **2011**, *196*, 2433-2444.

[10] Y. Qiao, C. M. Li, *J. Mater. Chem.* **2011**, *21*, 4027-4036.

[11] C. Bianchini, P. K. Shen, *Chem. Rev.* **2009**, *109*, 4183-4206.

[12] W. Li, in *Materials for Low- Temperature Fuel Cells*, (Eds: B. Ladewig, S. P. Jiang, Y. Yan), Wiley- VCH, Weinheim, Germany **2014**, Ch. 4.

[13] K. E. Toghill, R. G. Compton, *Int. J. Electrochem. Sci.* **2010**, *5*, 1246-1301.

[14] K. Dhara, D. R. Mahapatra, *Microchim Acta* **2018,** *185,* 49.

[15] L. Wang, A. Lavacchi, M. Bevilacqua, M. Bellini, P. Fornasiero, J. Filippi, M. Innocenti, A. Marchionni, H. A. Miller, F. Vizza, *ChemCatChem* **2015**, *7*, 2214-2221.

[16] Y. Lu, X. Feng, B. S. Takale, Y. Yamamoto, W. Zhang, M. Bao, *ACS Catal.* **2017**, *7*, 8296-8303.

[17] C. Chen, Q. Xie, D. Yang, H. Xiao, Y. Fu, Y. Tana, S. Yaoa, *RSC Adv.* **2013**, *3*, 4473-4491.

[18] S. Golunski, *Platinum Metals Rev.* **2007**, *51*, 162.

[19] E. Antolini, *Energy Environ. Sci.* **2009**, *2*, 915–931.

[20] E. Antolini, S. C. Zignani, S. F. Santos, E. R.Gonzalez, *Electrochim. Acta* **2011**, *56*, 2299-2305.

[21] B. D. Adams, A. Chen, *Mater. Today* **2011**, *14*, 282-289.

[22] G. A. Somorjai, *Chemistry in Two Dimensions: Surfaces,* Cornell University Press, Ithaca, NY, USA **1981**.

[23] X. Huang, S. Tang, X. Mu, Y. Dai, G. Chen, Z. Zhou, F. Ruan, Z. Yang and N. Zheng, *Nat. Nanotech.* **2011**, *6*, 28-32.

[24] P.-Y. Yang, S.-P. Ju, Z.-M. Lai, J.-S. Lin, J.-Y. Hsieh, *Nanoscale* **2016**, *8*, 2041-2045.

[25] A. Chen, C. Ostrom, *Chem. Rev.* **2015**, *115***,** 11999-12044.

[26] P. Ferrin, A. U. Nilekara, J. Greeley, M. Mavrikakis, J. Rossmeisl, *Surf. Sci.* **2008**, *602*, 3424-3431.

[27] W. Vogel, L. Lundquist, P. Ross, P. Stonehart, *Electrochim. Acta* **1975**, *20*, 79-93.

[28] J. Pala, T. Pal, *Nanoscale* **2015**, *7*, 14159-14190.

[29] J. Solla-Gullón, F. J. Vidal-Iglesiasa, J. M. Feliu, *Annu. Rep. Prog. Chem., Sect. C: Phys. Chem.* **2011**, *107*, 263-297.

[30] M. Crespo-Quesada, A. Yarulin, M. Jin, Y. Xia, L. Kiwi-Minsker, *J. Am. Chem. Soc.* **2011**, *133*, 12787–12794.

[31] E. Antolini, J. Perez, *J. Mater. Sci.* **2011,** *46,* 4435-4457.

[32] B. Lim, M. Jiang, J. Tao, P. H. C. Camargo, Y. Zhu, Y. Xia, *Adv. Funct. Mater.* **2009**, *19*, 189-200.

[33] Y. Li, Q. Liu, W. Shen, *Dalton Trans.* **2011**, *40*, 5811-5826.

[34] J. W. Hong, Y. Kim, Y. Kwon, S. W. Han, *Chem.-Asian J.* **2016**, *11*, 2224-2239.

[35] Y. Xia, X. Xia, H.-C. Peng, *J. Am. Chem. Soc.* **2015**, *137*, 7947–7966.

[36] H. Zhang, M. Jin, Y. Xiong, B. Lim, Y. Xia, *Acc. Chem. Res.* **2013**, *46*, 1783–1794.
[37] Z. Yin, L. Lin, D. Ma, *Catal. Sci. Technol.* **2014**, *4*, 4116-4128.
[38] N. Hoshi, M. Nakamura, H. Haneishi, *Electrochemistry* **2017**, *85*, 634–636.
[39] E. D. Wang, J. B. Xu, T. S. Zhao, *J. Phys. Chem. C* **2010**, *114*, 10489–10497.
[40] Z. Quan, Y. Wang, J. Fang, *Acc. Chem. Res.* **2013**, *46*, 191-202.
[41] J. N. Tiwari, R. N. Tiwari, K. S. Kim, *Prog. Mater. Sci.* **2012**, *57*, 724–803.
[42] D. Y. Chung, H. Shin, J. Y. Yoo, K.-S. Lee, N.-S. Lee, K. Kang, Y.-E. Sung, *J. Power Sources* **2016**, *334*, 52-57.
[43] L. M. Falicov, G. A. Somorjai, *Proc. Natl. Acad. Sci. USA* **1985**, *82*, 2207-2211.
[44] R. Huang, Y.-H Wen, Z.-Z. Zhua, S.-G. Sun, *J. Mater. Chem.* **2011**, *21*, 11578-11584.
[45] D. Yuan, X. Gong, R. Wu, *Phys. Rev. B* **2007**, *75*, 233401-233404.
[46] E. Pizzutilo, S. J. Freakley, S. Geiger, C. Baldizzone, A. Mingers, G. J. Hutchings, K. J. J. Mayrhofer, S. Cherevko, *Catal. Sci. Technol.* **2017**, *7*, 1848-1856.
[47] D. A. Slanac, W. G. Hardin, K. P. Johnston, K. J. Stevenson, *J. Am. Chem. Soc.* **2012,** *134*, 9812–9819.
[48] W. Wang, F. Lv, B. Lei, S. Wan, M. Luo, S. Guo, *Adv. Mater.* **2016**, *28*, 10117-10141.
[49] D. Deng, K. S. Novoselov, Q. Fu, N. Zheng, Z. Tian, X. Bao, *Nat. Nanotechnol.* **2016**, *11*, 218-230.
[50] C. Wen, Y. Wei, D. Tang, B. Sa, T. Zhang, C. Chen, *Sci. Rep.* **2017**, *7*, 1-11.
[51] Q. Li, S. Sun, *Nano Energy* **2016**, *29*, 178-197.
[52] Y. Xia, Y. Xiong, B. Lim, S. E. Skrabalak, *Angew. Chem. Int. Ed.* **2008**, *48*, 60-103.
[53] H. You, S. Yang, B. Dinga, H. Yang, *Chem. Soc. Rev.* **2013**, *42*, 2880-2904.
[54] W. Niu, L. Zhang, G. Xu, *ACS Nano* **2010**, *4*, 1987-1996.
[55] S.-H. Yoo, J.-H. Lee, B. Delley, A. Soon, *Phys. Chem. Chem. Phys*. **2014**, *16*, 18570-18577.
[56] Y. Xiong, Y. Xia, *Adv Mater.* **2007,** *19*, 3385-3391.
[57] S.-Y. Liu, Y.-T. Shen, C.-Y. Chiu, S. Rej, P.-H. Lin, Y.-C. Tsao, M. H. Huang, *Langmuir* **2015**, *31*, 6538−6545.
[58] J. Zhang, C. Feng, Y. Deng, L. Liu, Y. Wu, B. Shen, C. Zhong, W. Hu, *Chem. Mater*. **2014**, *26*, 1213−1218.
[59] F. J. Vidal-Iglesias, R. M. Arán-Ais, J. Solla-Gullón, E. Garnier, E. Herrero, A. Aldaz, J. M. Feliu, *Phys. Chem. Chem. Phys.* **2012**, *14*, 10258-10265.
[60] X. Xie, G. Gao, Z. Pan, T. Wang, X. Meng, L. Cai, *Sci. Rep.* **2015**, *5*, 1-5.
[61] L. Wei, C.-D. Xu, L. Huang, Z.-Y. Zhou, S.-P. Chen, S.-G. Sun, *J. Phys. Chem. C* **2016**, *120*, 15569-15577.
[62] Y. Zhang, M. Wang, E. Zhu, Y. Zheng, Y. Huang, X. Huang, *Nano Lett.* **2015**, *15*, 7519-7525.
[63] W. Niu, W. Zhang, S. Firdoz, X. Lu, *Chem. Mater.* **2014**, *26*, 2180-2186.
[64] N. Su, X. Chen, Y. Ren, B. Yue, H. Wang, W. Cai, H. He, *Chem. Commun.* **2015**, *51*, 7195-7198.
[65] Y. Wang, H.-C. Peng, J. Liu, C. Z. Huang, Y. Xia, *Nano Lett.* **2015**, *15*, 1445-1450.
[66] C.-H. Kuo, L. K. Lamontagne, C. N. Brodsky, L.-Y. Chou, J. Zhuang,B. T. Sneed, M. K. Sheehan, C.-K. Tsung, *ChemSusChem* **2013**, *6*, 1993-2000.
[67] D. A. Gilbert, E. C. Burks, S. V. Ushakov, P. Abellan, I. Arslan, T. E. Felter, A. Navrotsky, K. Liu, *Chem. Mater.* **2017**, *29*, 9814-9818.
[68] C. Koenigsmann, S. S. Wong, *Energy Environ. Sci.* **2011**, *4*, 1161-1176.
[69] H. Meng, C. Wang, P. K. Shen, G. Wu, *Energy Environ. Sci.* **2011**, *4*, 1522-1526.
[70] C. Xu, H. Wang, P.K. Shen, S. P. Jiang, *Adv. Mater.* **2007**, *19*, 4256-4259.

[71] Y. Wang, S.-I. Choi, X. Zhao, S. Xie, H.-C. Peng, M. Chi, C. Z. Huang, Y. Xia, *Adv. Funct. Mater.* **2014**, *24*, 131-139.

[72] L. Xiao, L. Zhuang, Y. Liu, J. Lu, H. D. Abruña, *J. Am. Chem. Soc.* **2009**, *131*, 602-608.

[73] A. K. Das, N. H. Kim, D. Pradhan, D. Hui, J. H. Lee, *Composites, Part B* **2018**¸ *144*, 11-18.

[74] S. Y. Tee, C. P. Teng, E. Ye, *Mater. Sci. Eng., C* **2017**, *70*, 1018-1030.

[75] Q. Wang, Q. Wang, K. Qi, T. Xue, C. Liu, W. Zheng, X. Cui, *Anal. Methods* **2015**, *7*, 8605-8610.

[76] M. A. Z. G. Sial, M. A. U. Din, X. Wang, *Chem. Soc. Rev*. **2018**, *47*, 6175-6200,

[77] M. N. Nadagouda, V. Polshettiwar, R. S. Varma, *J. Mater. Chem*. **2009**, *19*, 2026-2031.

[78] F. Jia, K.-w. Wong, R. Du, *Electrochem. Commun.* **2009**, *11*, 519-521.

[79] X. Yin, M. Shi, K. S. Kwok, H. Zhao, D. L. Gray, J. A. Bertke, H. Yang, *Nano Res.* **2018**, *11*, 3442–3452.

[80] D. Xu, Y. Liu, S. Zhao, Y. Lu, M. Han, J. Bao, *Chem. Commun.* **2017**, *53*, 1642-1645.

[81] X. Yin, X. Liu, Y.-T. Pan, K. A. Walsh, H. Yang, *Nano Lett.* **2014**, *14*, 7188-7194.

[82] W. Zhu, L. Zhang, P. Yang, C. Hu, Z. Luo, X. Chang, Z. Zhao, J. Gong, *Angew. Chem. Int. Ed.* **2018**, *57*, 1-6.

[83] X. Zhang, C. Lian, Z. Chen, C. Chen, Y. Li, *Nano Res.* **2018,** *11*, 4142-4148.

[84] H. Shan, L. Liu, J. He, Q. Zhang, W. Chen, R. Feng, C. Chang, P. Zhang, P. Tao, C. Song, W. Shang, T. Deng, J. Wu, *CrystEngComm* **2017**, *19*, 3439-3444.

[85] H. Wang, X. He, Y. Zhao, J. Li, T. Huang, H. Liu, *CrystEngComm* **2017**, *19*, 4304-4311.

[86] K. Gu, X. Pan, W. Wang, J. Ma, Y. Sun, H. Yang, H. Shen, Z. Huang, H. Liu, *Small* **2018**, *14*, 1801812.

[87] M. Farsadrooh, J. Torrero, L. Pascual, M. A. Peña, M. Retuerto, S. Rojas, *Appl. Catal., B* **2018**, *237*, 866-875.

[88] D. Xu, X. Liu, H. Lv, Y. Liu, S. Zhao, M. Han, J. Bao, J. He, B. Liu, *Chem. Sci.* **2018**, *9*, 4451-4455.

[89] X. Qiu, H. Zhang, P. Wu, F. Zhang, S. Wei, D. Sun, L. Xu, Y. Tang, *Adv. Funct. Mater.* **2017**, *27*, 1603852.

[90] M. Davi, D. Keßler, A. Slabon, *Thin Solid Films* **2016**, *615*, 221-225.

[91] B. Cai, V. Sayevich, N. Gaponik, A. Eychmüller, *Adv. Mater.* **2018***, 30,* 1707518.

[92] N. C. Bigall, A.-K. Herrmann, M. Vogel, M. Rose, P. Simon, W. Carrillo-Cabrera, D. Dorfs, S. Kaskel, N. Gaponik, A. *Eychmüller, Angew. Chem. Int. Ed. **2009**,* 48*, 9731-9734.*

[93] W. Liu, A.-K. Herrmann, N. C. Bigall, P. Rodriguez, D. Wen, M. Oezaslan, T. J. Schmidt, N. Gaponik, A. Eychmüller, *Acc. Chem. Res.* **2015**, *48*, 154-162.

[94] A. Mohanty, N. Garg, R. Jin, *Angew. Chem. Int. Ed.* **2010**, *49*, 4962-4966.

[95] V. Malgras, H. Ataee-Esfahani, H. Wang, B. Jiang, C. Li, K. C.-W. Wu, J. H. Kim, Y. Yamauchi, *Adv. Mater.* **2016**, *28*, 993-1010.

[96] J. Zhang, C. M. Li, *Chem. Soc. Rev.* **2012**, *41*, 7016-7031.

[97] S. Tominaka, S. Ohta, H. Obata, T. Momma, T. Osaka, *J. Am. Chem. Soc.* **2008**, *130*, 10456-10457.

[98] X. Niu, M. Lan, H. Zhao, C. Chen, *Anal. Chem.* **2013**, *85*, 3561-3569.

[99] S.A. Al-Muhtaseb, J.A. Ritter, *Adv. Mater.* **2003**, *15*, 101-114.

[100] S. D. Minteer, B. Y. Liaw, M. J. Cooney, *Curr. Opin. Biotechnol.* **2007**, *18*, 228-234.

[101] Y. Kamitaka, S. Tsujimura, N. Setoyama, T. Kajino, K. Kano, *Phys. Chem. Chem. Phys.* **2007**, *9*, 1793-1801.

[102] D. Wen, A.-K. Herrmann, L. Borchardt, F. Simon, W. Liu, S. Kaskel, A. Eychmüller, *J. Am. Chem. Soc.* **2014**, *136*, 2727-2730.

[103] F. J. Burpo, E. A. Nagelli, L. A. Morris, J. P. McClure, M. Y. Ryu, J. L. Palmer, *J. Mater. Res.* **2017**, *32*, 4153-4165.
[104] M. Z. Yazdan-Abad, M. Noroozifar, A. R. M. Alam, H. Saravani, *J. Mater. Chem. A* **2017**, *5*, 10244-10249.
[105] A. S. Douk, H. Saravani, M. Noroozifar, *Electrochim. Acta* **2018,** *275*, 182-191.
[106] P. Zhou, Z. Dai, M. Fang, X. Huang, J. Bao, J. Gong, *J. Phys. Chem. C* **2007**, *111*, 12609-12616.
[107] S. Patra, B. Viswanath, K. Barai, N. Ravishankar, N. Munichandraiah, *ACS Appl. Mater. Interfaces* **2010**, *2*, 2965-2969.
[108] F. Yang, K. Cheng, Y. Mo, L. Yu, J. Yin, G. Wang, D. Cao, *J. Power Sources* **2012**, *217*, 562-568.
[109] Y. Zhao, S.-J. Qin, Y. Li, F.-X. Deng, Y.-Q. Liu, G.-B. Pan, *Electrochim. Acta* **2014**, *145*, 148-153.
[110] A. J. Bard, L. R. Faulkner, *Electrochemical Methods: Fundamental and Applications*, 2nd ed., John Wiley & Sons, Hoboken, NJ, **2001**.
[111] J. Bai, L. Shen, D. Sun, Y. Tang, T. Lu, *CrystEngComm* **2014**, *16*, 10445-10450.
[112] W. Du, K. E. Mackenzie, D. F. Milano, N. A. Deskins, D. Su, X. Teng, *ACS Catal.* **2012**, *2*, 287-297.
[113] Y. Liu, J. Goebla, Y. Yin, *Chem. Soc. Rev.* **2013**, *42*, 2610-2653.
[114] S. Yang, X. Luo, *Nanoscale* **2014**, *6*, 4438-4457.
[115] X.-Y. Yang, L.-H. Chen, Y. Li, J. C. Rooke, C. Sanchez, B.-L. Su, *Chem. Soc. Rev.* **2017**, *46*, 481-558.
[116] N. Menzel, E. Ortel, R. Kraehnert, P. Strasser, *ChemPhysChem* **2012**, *13*, 1385-1394.
[117] J.-G. Li, C.-Y. Tsai, S.-W. Kuo, *RSC Adv.* **2015**, *5*, 42798-42803.
[118] C. Zhu, D. Du, A. Eychmüller, Y. Lin, *Chem. Rev.* **2015**, *115*, 8896-8943.
[119] L. Ye, Y. Wang, X. Chen, B. Yue, S. C. Tsang, H. He, *Chem. Commun.* **2011**, *47*, 7389-7391.
[120] X. Chen, Z. Lou, M. Qiao, K. Fan, S. C. Tsang, H. He, *J. Phys. Chem. C* **2008**, *112*, 1316-1320.
[121] D. Y. Zhao, J. L. Feng, Q. S. Huo, N. Melosh, G. H. Fredrickson, B. F. Chmelka, G. D. Stucky, *Science* **1998**, *279*, 548-552.
[122] K. K. Zhu, B. Yue, W. Z. Zhou, H. Y. He, *Chem. Commun.* **2003**, *1*, 98-99.
[123] Y. Wang, N. Su, L. Ye, Y. Ren, X. Chen, Y. Du, Z. Li, B. Yue, S. Chi, E. Tsang, Q. Chen, H. He, *J. Catal.* **2014**, *313*,113-126.
[124] N. Su, X. Chen, B. Yue, H. He, *Catal. Sci. Technol.* **2015**, *5*, 638-649.
[125] C. Wang, D. Chen, X. Jiao, *Sci. Technol. Adv. Mater.* **2009**, *10,* 023001.
[126] Y. Yamauchi, K. Kuroda, *Chem.-Asian J.* **2008**, *3*, 664-676.
[127] P. N. Bartlett, J. Marwan, *Chem. Mater.* **2003**, *15*, 2962-2968.
[128] P. J. Cappillino, K. M. Hattar, B. G. Clark, R. J. Hartnett, V. Stavila, M. A. Hekmaty, B. W. Jacobs, D. B. Robinson, *J. Mater. Chem. A* **2013**, *1*, 602-610.
[129] K. Qi, Q. Wang, W. Zheng, W. Zhang, X. Cui, *Nanoscale* **2014**, *6*, 15090-15097.
[130] L. Zhang, J. Zhang, Z. Jiang, S. Xie, M. Jin, X. Han, Q. Kuang, Z. Xie, L. Zheng, *J. Mater. Chem.* **2011**, *21*, 9620-9625.
[131] Y. Wu, G. Li, L. Zou, S. Lei, Q. Yu, B. Ye, *Sens. Actuators, B* **2018**, *259*, 372-379.
[132] C. Li, T. Sato, Y. Yamauchi, *Chem. Commun.* **2014**, *50*, 11753-11756.
[133] C. Li, B. Jiang, M. Imura, N. Umezawa, V. Malgras, Y. Yamauchi, *Chem.-Eur. J.* **2015**, *21*, 18671-18676.
[134] C. Li, B. Jiang, N. Miyamoto, J. H. Kim, V. Malgras, Y. Yamauchi, *J. Am. Chem. Soc.* **2015**, *137*, 11558-11561.
[135] B. Jiang, C. Li, H. Qian, M. S. A. Hossain, V. Malgras, Y. Yamauchi, *Angew. Chem. Int. Ed.* **2017**, *56*, 7836-7841.

[136] Y. Li, B. P. Bastakoti, Y. Yamauchi, *APL Mater.* **2016**, *4*, 040703-1-8.
[137] S. J. Ye, D. Y. Kim, S. W. Kang, K. W. Choi, S. W. Han, O O. Park, *Nanoscale* **2014**, *6*, 4182-4187.
[138] E. Antolini, *Appl. Catal., B* **2017**, *217*, 201–213.
[139] N. Kakati, J. Maiti, S. H. Lee, S. H. Jee, B. Viswanathan, Y. S. Yoon, *Chem. Rev.* **2014**, *114*, 12397-12429.
[140] K. D. Gilroy, A. Ruditskiy, H.-C. Peng, D. Qin, Y. Xia, *Chem. Rev.* **2016**, *116*, 10414-10472.
[141] B. J. Plowman, I. Najdovski, A. Pearson, A. P. O'Mullane, *Faraday Discuss.* **2013**, *164*, 199-218.
[142] M. Sankar, N. Dimitratos, P. J. Miedziak, P. P. Wells, C. J. Kielye, G. J. Hutchings, *Chem. Soc. Rev.* **2012**, *41*, 8099-8139.
[143] S. Shan, J. Luo, J. Wu, N. Kang, W. Zhao, H. Cronk, Y. Zhao, P. Joseph, V. Petkov, C.-J. Zhong, *RSC Adv.* **2014**, *4*, 42654-42669.
[144] H.-l. Liu, F. Nosheen, X. Wang, *Chem. Soc. Rev.* **2015**, *44*, 3056-3078.
[145] Y. Xu, L. Chen, X. Wang, W. Yao, Q. Zhang, *Nanoscale* **2015**, *7*, 10559-10583.
[146] L. Zhang, Q. Chang, H. Chen, M. Shao, *Nano Energy* **2016**, *29*, 198-219.
[147] C. Ray, T. Pal, *J. Mater. Chem. A* **2017**, *5*, 9465-9487.
[148] M. H. Seo, S. M. Choi, D. U. Lee, W. B. Kim, Z. Chen, *J. Power Sources* **2015**, *300*, 1-9.
[149] L. Chen, L. Lu, H. Zhu, Y. Chen, Y. Huang, Y. Li, L. Wang, *Nat. Commun.* **2016**, *8*, 14136.
[150] Y. Yazawa, H. Yoshida, N. Takagi, S. Komai, A. Satsuma, T. Hattori, *Appl. Catal., B* **1998**, *19*, 261-266.
[151] W. Xiao, W. Lei, M. Gong, H. L. Xin, D. Wang, *ACS Catal.* **2018**, *8*, 3237-3256.
[152] J. Xue, G. Han, W. Ye, Y. Sang, H. Li, P. Guo, X. S. Zhao, *ACS Appl. Mater. Interfaces* **2016**, *8*, 34497-34505.
[153] A. K. Singh, Q. Xu, *ChemCatChem* **2013**, *5*, 652-676.
[154] N. Lopez, J. K. Nørskov, *Surf. Sci.* **2001**, *477*, 59-75.
[155] Z. X. Liang, T. S. Zhao, J. B. Xu, L. D. Zhu, *Electrochim. Acta* **2009**, *54*, 2203–2208.
[156] E. A. Monyoncho, S. N. Steinmann, C. Michel, E. A. Baranova, T. K. Woo, P. Sautet, *ACS Catal.* **2016**, *6*, 4894-4906.
[157] E. A. Monyoncho, S. N. Steinmann, P. Sautet, E. A. Baranova, C. Michel, *Electrochim. Acta* **2018**, *274*, 274-278.
[158] M. Li, W. Guo, R. Jiang, L. Zhao, H. Shan, *Langmuir* **2010**, *26*, 1879-1888.
[159] S. Sarkar, R. Jana, Suchitra, U. V. Waghmare, B. Kuppan, S. Sampath, S. C. Peter, *Chem. Mater.* **2015**, *27*, 7459-7467.
[160] Q. Shi, C. Zhu, C. Bi, H. Xia, M. H. Engelhard, D. Du, Y. Lin, *J. Mater. Chem. A* **2017**, *5*, 23952-23959.
[161] R. Jana, U. Subbarao, S. C. Peter, *J. Power Sources* **2016**, *301*, 160-169.
[162] H. Liao, J. Zhu, Y. Hou, *Nanoscale* **2014**, *6*, 1049-1055.
[163] V. Mazumder, M. Chi, M. N. Mankin, Y. Liu, Ö. Metin, D. Sun, K. L. More, S. Sun, *Nano Lett.* **2012**, *12*, 1102-1106.
[164] S. Tominaka, T. Hayashi, Y. Nakamura, T. Osaka, *J. Mater. Chem.* **2010**, *20*, 7175-7182.
[165] J.-N. Zheng, L.-L. He, F.-Y. Chen, A.-J. Wang, M.-W. Xue, J.-J. Feng, *J. Mater. Chem. A* **2014**, *2*, 12899-12906.
[166] Y. Ma, R. Wang, H. Wang, J. Key, S. Ji, *RSC Adv.* **2015**, *5*, 9837-9842.
[167] D. Chen, P. Sun, H. Liu, J. Yang, *J. Mater. Chem. A* **2017**, *5*, 4421-4429.
[168] J. Liu, Z. Huang, K. Cai, H. Zhang, Z. Lu, T. Li, Y. Zuo, H. Han, *Chem.-Eur. J.* **2015**, *21*, 17779-17785.

[169] Y. Chen, Y. Yang, G. Fu, L. Xu, D. Sun, J.-M. Lee, Y. Tang, *J. Mater. Chem. A* **2018**, *6*, 10632-10638.
[170] C. Zhu, Q. Shi, S. Fu, J. Song, H. Xia, D. Du, Y. Lin, *Adv. Mater.* **2016**, *28*, 8779-8783.
[171] B. Yan, C. Wang, H. Xu, K. Zhang, S. Li, Y. Du, *ChemPlusChem* **2017**, *82*, 1121-1128.
[172] L. Yang, C. Hu, J. Wang, Z. Yang, Y. Guo, Z. Bai, K. Wang, *Chem. Commun.* **2011**, *47*, 8581-8583.
[173] Y. Xiong, W. Ye, W. Chen, Y. Wu, Q. Xu, Y. Yan, H. Zhang, J. Wu, D. Yang, *RSC Adv.* **2017**, *7*, 5800-5806.
[174] L. Zhang, S.-I. Choi, J. Tao , H.-C. Peng, S. Xie, Y. Zhu, Z. Xie, Y. Xia, *Adv. Funct. Mater.* **2014**, *24*, 7520-7529.
[175] J. Fan, S.Yu, K. Qi, C. Liu, L. Zhang, H. Zhang, X. Cui, W. Zheng, *J. Mater. Chem. A* **2018**, *6*, 8531-8536.
[176] D. Chen, Q. Yao, P. Cui, H. Liu, J. Xie, J. Yang, *ACS Appl. Energy Mater.* **2018**, *1*, 883-890.
[177] B. Jiang, C. Li, V. Malgras, Y. Bando, Y. Yamauchi, *Chem. Commun.* **2016**, *52*, 1186-1189.
[178] K. Jiang, P. Wang, S. Guo, X. Zhang, X. Shen, G. Lu, D. Su, X. Huang, *Angew. Chem.* **2016**, *128*, 9176-9181.
[179] K. Mori, K. Naka, S. Masuda, K. Miyawaki, H. Yamashita, *ChemCatChem* **2017**, *9*, 3456-3462.
[180] D. Bin, B. Yang, F. Ren, K. Zhang, P. Yang, Y. Du, *J. Mater. Chem. A* **2015**, *3*, 14001-14006.
[181] B. Cai, D. Wen, W. Liu, A.-K. Herrmann, A. Benad, A. Eychmüller, *Angew. Chem. Int. Ed.* **2015**, *54*, 13101-13105.
[182] Z. Liu, X. Yang, L. Cui, Z. Shi, B. Lu, X. Guo, J. Zhang, L. Xu, Y. Tang, Y. Xiang, *Part. Part. Syst. Charact.* **2017**, *35*, 1700366.
[183] C. Zhu, D. Wen, M. Oschatz, M. Holzschuh, W. Liu, A.-K. Herrmann, F. Simon, S. Kaskel, A. Eychmüller, *Small* **2015**, *11*, 1430-1434.
[184] C. Du, M. Chen, W. Wang, G. Yin, *ACS Appl. Mater. Interfaces* **2011**, *3*, 105-109.
[185] J. Zhang, Y. Xu, B. Zhang, *Chem. Commun.* **2014**, *50*, 13451-13453.
[186] C. Zhu, Q. Shi, S. Fu, J. Song, D. Du, D. Su, M. H. Engelhard, Y. Lin, *J. Mater. Chem. A* **2018**, *6*, 7517-7521.
[187] L.-X. Ding, A.-L. Wang, Y.-N. Ou, Q. Li, R. Guo, W.-X. Zhao, Y.-X. Tong, G.-R. Li, *Sci. Rep.* **2013**, *3*, 1-7.
[188] W. Hong, J. Wang, E. Wang, *CrystEngComm* **2015**, *17*, 9011-9015.
[189] X. Wang, S. Wang, in *Materials for Low-Temperature Fuel Cells*, (Eds: B. Ladewig, S. P. Jiang, Y. Yan), Wiley-VCH, Weinheim, Germany **2014**, Ch. 3.
[190] Q.-L. Zhu, Q. Xu, *Chem.* **2016**, *1*, 220-245.
[191] E. Pérez-Mayoral, V. Calvino-Casildaa, E. Soriano, *Catal. Sci. Technol.* **2016**, *6*, 1265-1291.
[192] H. Ali, S. Zaman, I. Majeed, F. K. Kanodarwala, M. A. Nadeem, J. A. Stride, M. A. Nadeem, *ChemElectroChem* **2017**, *4*, 3126–3133.
[193] S. Hu, F. Munoz, J. Noborikawa, J. Haan, L. Scudiero, S. Ha, *Appl. Catal., B* **2016**, *180*, 758-765.
[194] X. Liu, P. Ning, L. Xu, Q. Liu, Z. Song, Q. Zhang, *RSC Adv.* **2016**, *6*, 41181-41188.
[195] H. Yan, Z. Bai, S. Chao, L. Yang, Q. Cui, K. Wang, L. Niu, *RSC Adv.* **2013**, *3*, 20332-20337.
[196] Z. Zhang, C. Zhang, J. Sun, T. Kou, Q. Bai, Y. Wang, Y. Ding, *J. Mater. Chem. A* **2013**, *1*, 3620-3628.
[197] A. L. Bugaev, A. A. Guda, A. Lazzarini, K. A. Lomachenko, E. Groppo, R. Pellegrini, A. Piovano, H. Emerich, A. V. Soldatov, L. A. Bugaev, V. P. Dmitriev, J. A. van Bokhoven, C. Lamberti, *Catal. Today* **2017**, *283*, 119-126.

[198] J. Yang, Y. Xie, R. Wang, B. Jiang, C. Tian, G. Mu, J. Yin, B. Wang, H. Fu, *ACS Appl. Mater. Interfaces* **2013**, *5*, 6571-6579.
[199] C. He, J. Tao, Y. Kea, Y. Qiu, *RSC Adv.* **2015**, *5*, 66695-66703.
[200] S. Ghosh, A.-L. Teillout, D. Floresyona, P. de Oliveira, A. Hagège, H. Remita, *Int. J. Hydrog. Energy* **2015**, *40*, 4951-4959.
[201] R. K. Pandey, V. Lakshminarayanan, *J. Phys. Chem. C* **2010**, *114*, 8507-8514.
[202] S. Ghosh, S, Bera, S. Bysakh, R. N. Basu, *ACS Appl. Mater. Interfaces* **2017**, *9*, 33775-33790.
[203] S. Siwal, S. Matseke, S. Mpelane, N. Hooda, D. Nandi, K. Mallick, *Int. J. Hydrog. Energy* **2017**, *42*, 23599-23605.
[204] L. A. Fard, R. Ojani, J. B. Raoof, E. N. Zare, M. M. Lakouraj, *Energy* **2017**, *127*, 419-427.
[205] Z. Łodziana, J. K. Nørskov, *Surf. Sci.* **2002**, *518*, 577–582.
[206] Y.-J. Wang, D. P. Wilkinson, J. Zhang, *Chem. Rev.* **2011**, *111*, 7625-7651.
[207] S. Ch. Sarma, S. C. Peter. *Dalton Trans.* **2018**, *47*, 7864-7869.
[208] R. G. Rao, R. Blume, T. W. Hansen, E. Fuentes, K. Dreyer, S. Moldovan, O. Ersen, D. D. Hibbitts, Y. J. Chabal, R. Schlögl, J.-P. Tessonnier, *Nat. Commun.* **2017**, *8*, 340.
[209] W. Xin, Y. Song, *RSC Adv.* **2015**, *5*, 83239-83285.
[210] M. Khan, M. N. Tahir, S. F. Adil, H. U. Khan, M. R. H. Siddiqui, A. A. Al-warthan, W. Tremel, *J. Mater. Chem. A* **2015**, *3*, 18753-18808.
[211] Q. Wang, Y. Liao, H. Zhang, J. Li, W. Zhao, S. Chen, *J. Power Sources* **2015**, *292*, 72-77.
[212] M. Shao, J. H. Odell, S.-I. Choi, Y. Xia, *Electrochem. Commun.* **2013**, *31*, 46–48.
[213] G. Z. Hu, F. Nitze, X. Jia, T. Sharifi, H. R. Barzegar, E. Gracia-Espino, T. Wågberg, *RSC Adv.* **2014**, *4*, 676-682.
[214] Q. Zhang, L. Jiang, H. Wang, J. Liu, J. Zhang, Y. Zheng, F. Li, C. Yao, S. Hou, *ACS Sustainable Chem. Eng.* **2018**, *6*, 7507-7514.
[215] H. Huang, X. Wang, *J. Mater. Chem.* **2012**, *22*, 22533-22541.
[216] D. Liu, Q. Guo, H. Hou, O. Niwa, T. You, *ACS Catal.* **2014**, *4*, 1825-1829.
[217] Z. Yan, W. Yao, L. Hu, D. Liu, C. Wang, C.-S. Lee, *Nanoscale* **2015**, *7*, 5563-5577.
[218] R. D. Morgan, A. Salehi-khojin, R. I. Masel, *J. Phys. Chem. C* **2011**, *115*, 19413-19418.
[219] S. Mondal, S. Ghosh, C. R. Raj, *ACS Omega* **2018**, *3*, 622-630.
[220] L. Y. Zhang, C. X. Guo, H. Pang, W. Hu, Y. Qiao, C. M. Li, *ChemElectroChem* **2014**, *1*, 72-75.
[221] H. Yang, X. Zhang, H. Zou, Z. Yu, S. Li, J. Sun, S. Chen, J. Jin, J. Ma, *ACS Sustainable Chem. Eng.* **2018**, *6*, 7918−7923.
[222] G. Hu, F. Nitze, T. Sharifi, H. R. Barzegar, T. Wågberg, *J. Mater. Chem.* **2012**, *22*, 8541-8548.
[223] X. Jia, G. Hu, F. Nitze, H. R. Barzegar, T. Sharifi, C.-W. Tai, T. Wågberg, *ACS Appl. Mater. Interfaces* **2013**, *5*, 12017-12022.
[224] B. F. Machadoab, P. Serp, *Catal. Sci. Technol.* **2012**, *2*, 54-75.
[225] M. Liu, R. Zhang, W. Chen, *Chem. Rev.* **2014**, *114*, 5117-5160.
[226] M. Sawangphruk, A. Krittayavathananon, N. Chinwipas, P. Srimuk, T. Vatanatham, S. Limtrakul, J. S. Foord, *Fuel Cells* **2013**, *13*, 881-888.
[227] H. Chang, H. Wu, *Energy Environ. Sci.* **2013**, *6*, 3483-3507.
[228] F. Ren, K. Zhang, D. Bin, B. Yang, H. Wang, P. Yang, Z. Fei, Y. Du, *ChemCatChem* **2015**, *7*, 3299-3306.
[229] R. Kiyani, M. J. Parnian, S. Rowshanzamir, *Int. J. Hydrog. Energy* **2017**, *42*, 23070-23084.
[230] Z. Liu, Y. Feng, X. Wu, K. Huang, S. Feng, X. Dong, Y. Yanga, B. Zhao, *RSC Adv.* **2016**, *6*, 98708-98716.

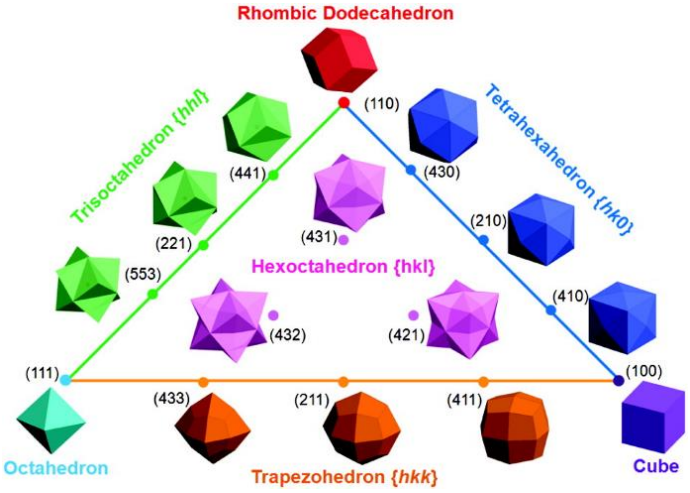

Figure 1. Triangular diagram showing the correlations between convex polyhedron with different crystallographic facets. Reproduced with permission.[37] Copyright 2014, The Royal Society of Chemistry.

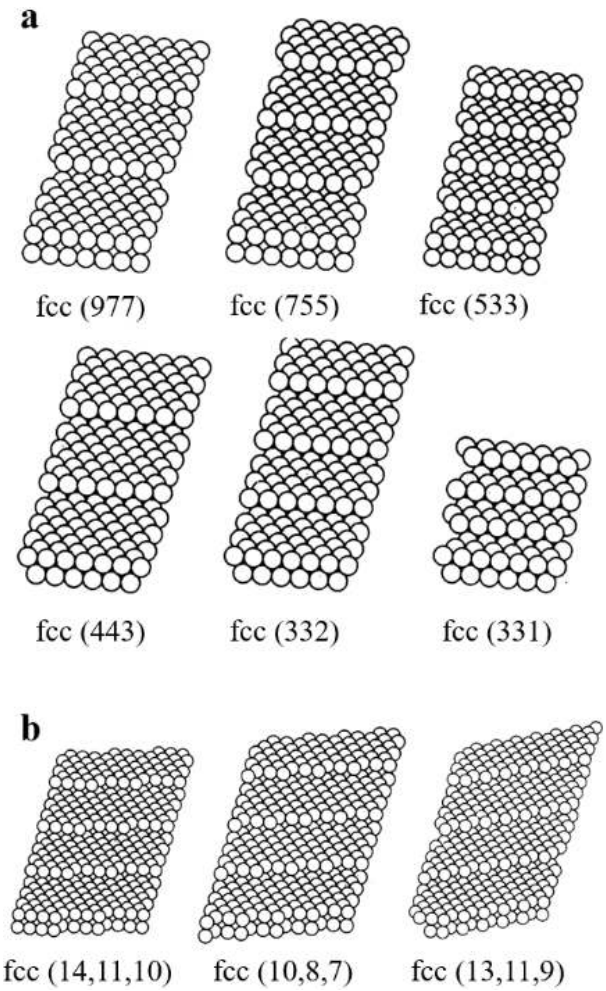

Figure 2. Various (a) stepped and (b) kinked surfaces in close-packed *fcc* lattice. Reproduced with permission.[43] Copyright 1985, US National Academy of Sciences.

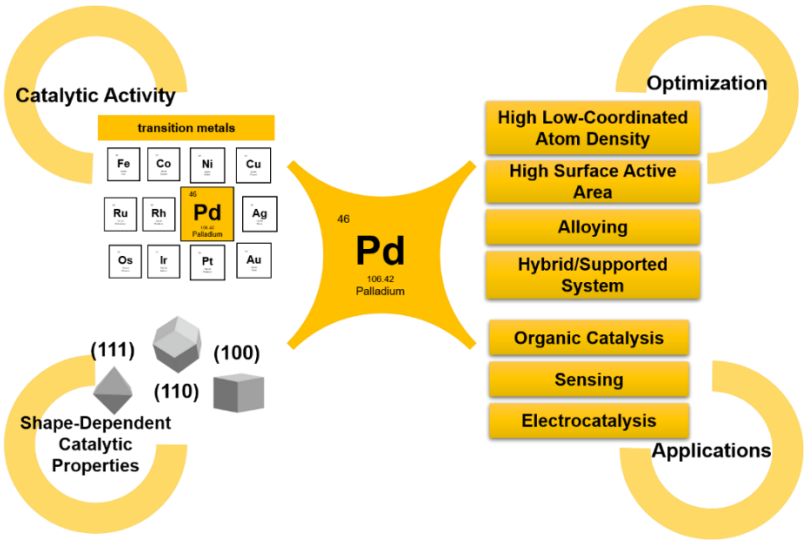

Figure 3. Schematic diagram of the basic concept of Pd as nanocatalyst. Pd belongs to the *d*-block transition metals and its high catalytic activity arises from the incompletely-filled subshell in the *d*-orbital. The catalytic performance of Pd-based catalysts has been shown to be dependent on the shape and size of the Pd nanocatalyst. The optimization to meet the demand for high performance Pd catalyst can be achieved by creating nanoarchitectures which possess a high density of low-coordinated atoms, high surface-active area, and high stability by combining Pd with other elements to provide synergistic effects. Various Pd nanoarchitectures are promising for many applications, such as organic catalysis, non-enzymatic sensing and electrocatalysis.

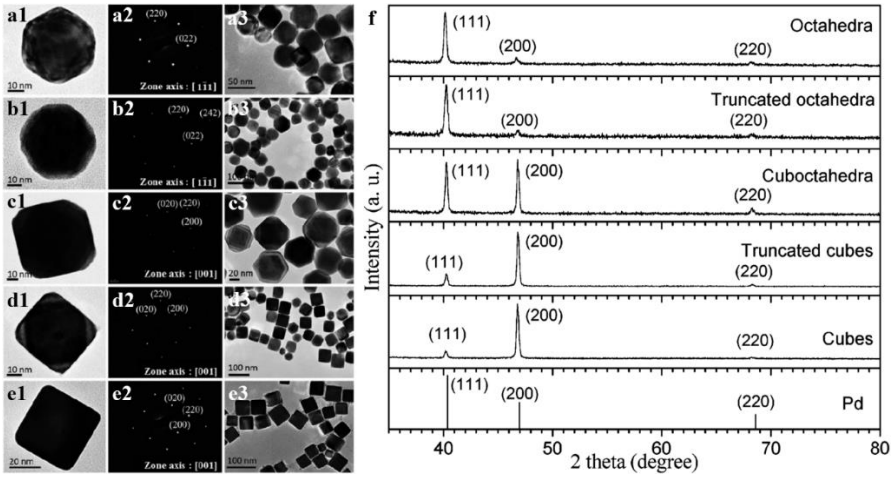

Figure 4. TEM images of single Pd nanocrystals, their corresponding SAED patterns and TEM images of the particles over larger areas: (a1-a3) Pd octahedra, (b1-b3) truncated octahedra, (c1-c3) cuboctahedra, (d1-d3) truncated cubes, and (e1-e3) cubes. The respective diffraction patterns for the various Pd nanocrystals are shown in panel (f). Reproduced with permission.[57] Copyright 2015, American Chemical Society.

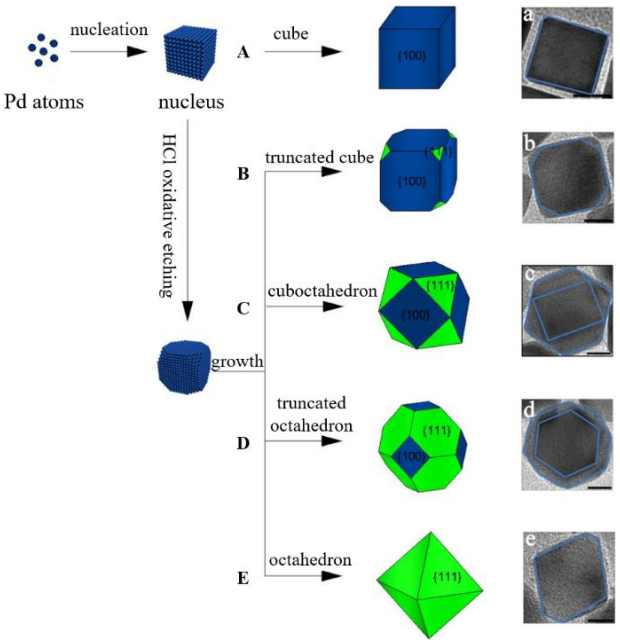

Figure 5. Schematic illustration of shape evolution of the Pd nanocrystals and (a-e) the corresponding TEM images for various morphologies, respectively (scale bars, 10 nm), where slight truncation at the corner of cubic Pd was induced by HCl oxidative etching in the early stage and then, continuous atomic addition to {100} facets promotes the enlargement of {111} facets, resulting in the formation of octahedral Pd bounded by {111} facets. Reproduced with permission.[58] Copyright 2014, The Royal Society of Chemistry.

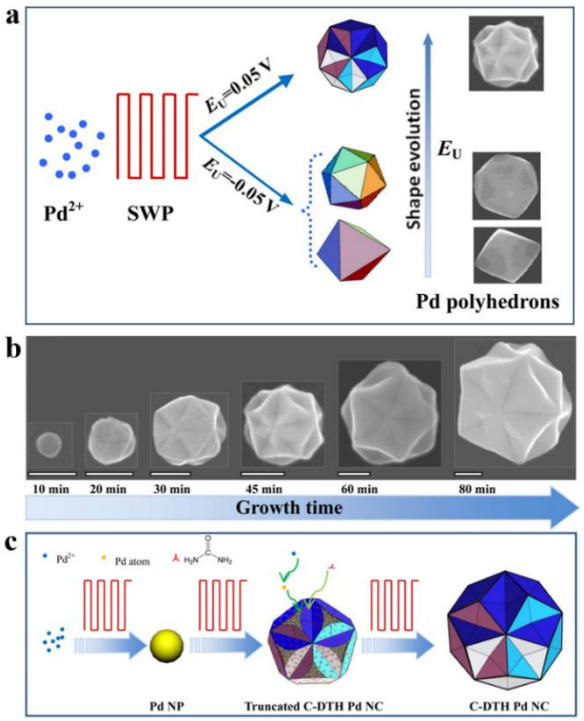

Figure 6. (a) Illustration of shape evolution of polyhedral Pd NCs by adjusting upper limit potential (E_U). (b) SEM images of Pd NPs electrodeposited on GCE for different time, showing the growth process of C-DTH Pd NCs. Scale bars are 100 nm. (c) Schematic illustration of the proposed growth mechanism of C-DTH Pd NCs. Reproduced with permission.[61] Copyright 2016, American Chemical Society.

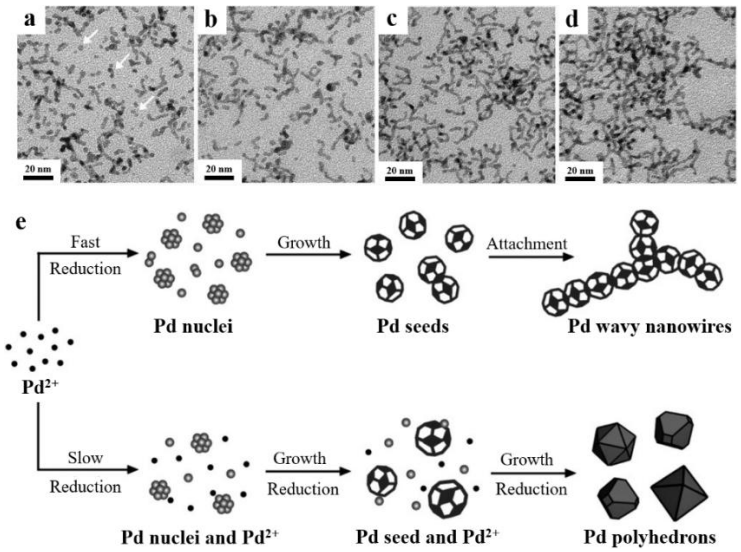

Figure 7. TEM images showing the attachment and time-dependent growth of Pd nanoparticles into wavy nanowires at 140 °C after the precursor had been injected: a) 1 min, b) 10 min, c) 30 min, and d) 3 h. The white arrows in (a) mark a few typical small Pd nanoparticles formed in the early stage of the synthesis. (e) A schematic illustration showing how the reaction kinetics (as mediated by precursor) affect the nucleation, growth, attachment, and thus, the final morphology of Pd nanostructures in polyol synthesis. Reproduced with permission.[71] Copyright 2014, Wiley-VCH Verlag GmbH.

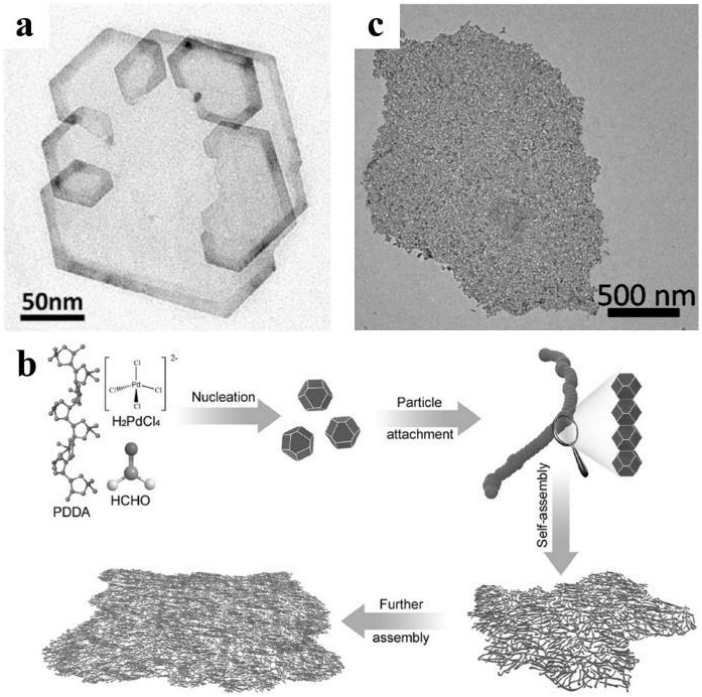

Figure 8. (a) TEM image of Pd nanosheets. Reproduced with permission.[67] Copyright 2015, American Chemical Society. (b) Schematic illustration of the possible formation mechanism and (c) TEM image of the free-standing 2D porous Pd nanosheets through particle attachment and self-assembly processes. Reproduced with permission.[89] Copyright 2017, Wiley-VCH Verlag GmbH.

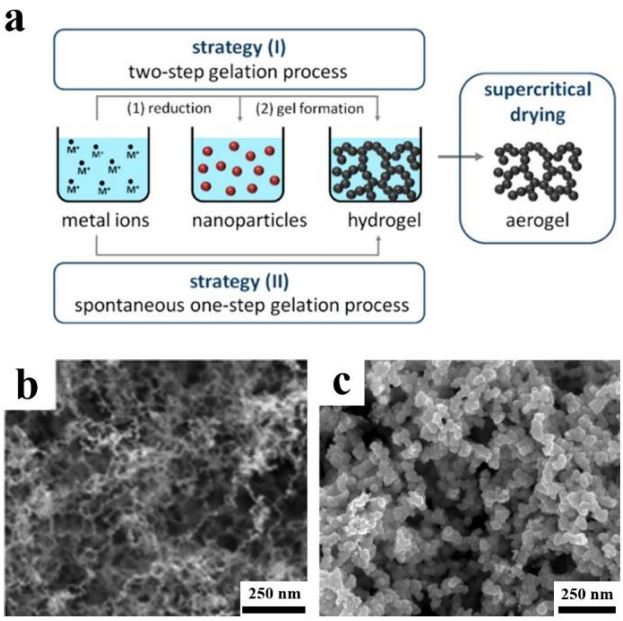

Figure 9. (a) Schematic illustration of noble metal aerogel preparation *via* gelation of pre-formed nanoparticles (Strategy (I)) and *via* an *in-situ* spontaneous gelation process (Strategy (II)). Reproduced with permission.[93] Copyright 2015, American Chemical Society. SEM images of Pd aerogels prepared using (b) Strategy I (Reproduced with permission.[102] Copyright 2014, American Chemical Society) and (c) Strategy II. Reproduced with permission.[103] Copyright 2017, Cambridge University Press.

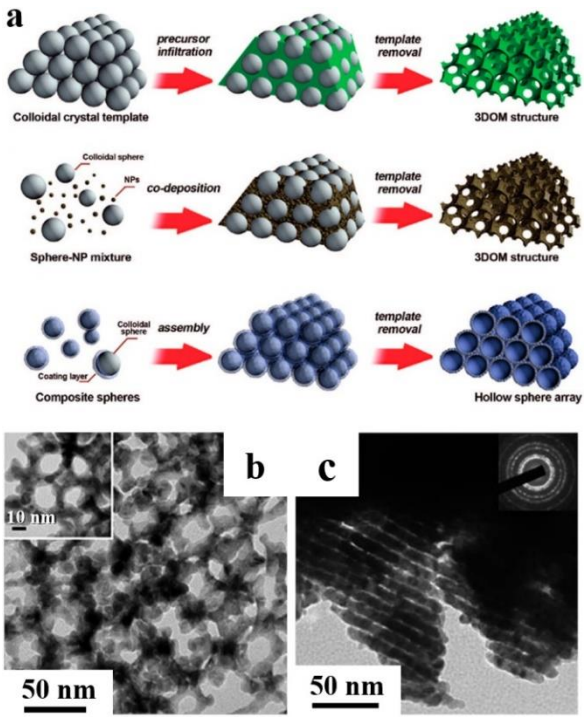

Figure 10. (a) Three different approaches for synthesizing ordered porous structures using colloidal crystal templating. Reproduced with permission.[118] Copyright 2015, American Chemical Society. TEM images of (b) silica-free 3DOM Pd networks recorded along zone axis ⟨100⟩ with an enlarged image (inset in b) Reproduced with permission.[119] Copyright 2011, The Royal Society of Chemistry, and (c) as-prepared silica-free hexagonally packed Pd nanoarray with the SAED pattern (inset in c). Reproduced with permission.[120] Copyright 2008, American Chemical Society.

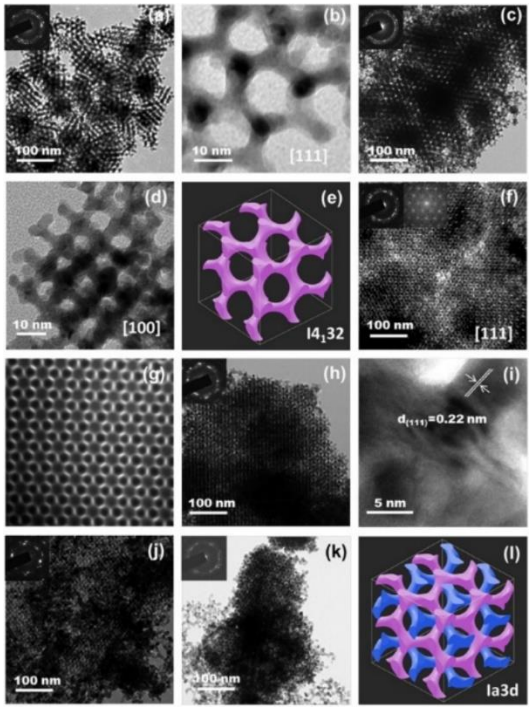

Figure 11. TEM images of silica-free mesoporous Pd network catalysts. Various KIT-6 templates were used: (a, b) Pd-308-KBH_4, (c, d) Pd-353-KBH_4, (e) skeletal model of a fragment of single gyroid with $I4_132$ symmetry, (f) Pd-373-KBH_4, (g) TEM image simulation of Pd-373-KBH_4, (h, i) Pd-403-KBH_4, (j) Pd-373-H_2, (k) Pd-373-$N_2H_4{\cdot}H_2O$ and (l) skeletal model of a fragment of double gyroid with *Ia3d* symmetry. Insets are the corresponding SAED patterns and Fourier diffractograms. Reproduced with permission.[123] Copyright 2014, Elsevier, Ltd.

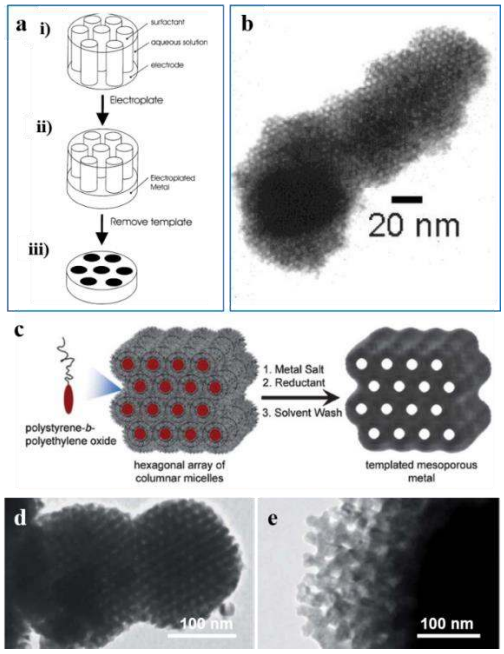

Figure 12. (a) Schematic representation of the templating process used to deposit the H_1-e films. The cylinders represent the micellar rods in the lyotropic liquid-crystalline phase. (b) TEM image of H_1-e palladium. Reproduced with permission.[127] Copyright 2003, American Chemical Society. (c) Scheme for the formation mechanism of PS-*b*-PEO templated mesoporous Pd. (d) Low- and (e) high-magnification TEM images of nanoporous Pd particles prepared using PS_{2300}-*b*-PEO_{3100} and PS_{3800}-*b*-PEO_{5000}, respectively. Reproduced with permission.[128] Copyright 2013, The Royal Society of Chemistry.

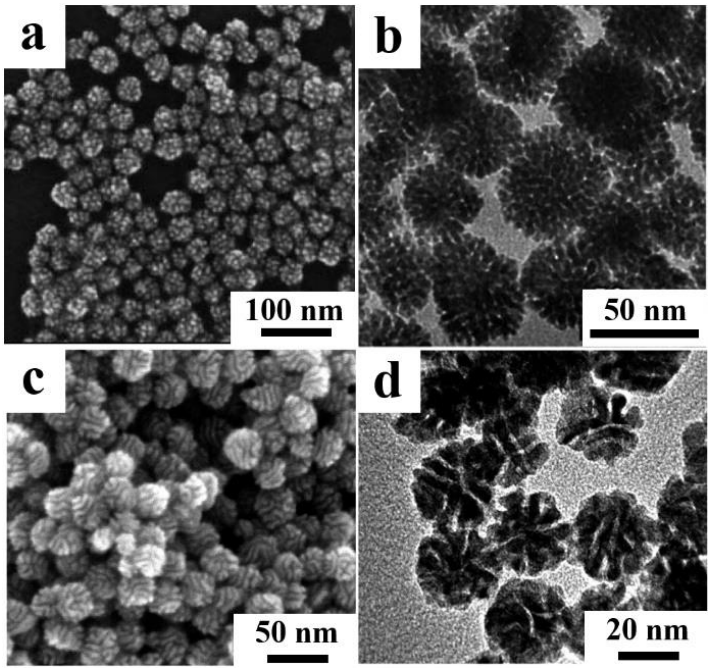

Figure 13. (a, c) SEM and (b, d) TEM images of mesoporous Pd particles prepared *via* chemical reduction with different structure-directing agents: (a, b) CTAC (Reproduced with permission.[130] Copyright 2011, The Royal Society of Chemistry) and (c, d) HDPC (Reproduced with permission.[132] Copyright 2014, The Royal Society of Chemistry)

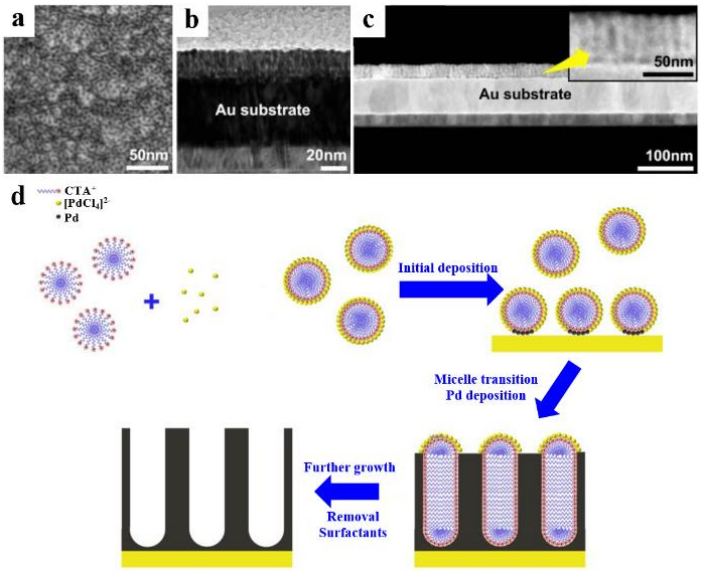

Figure 14. (a) Top view SEM image, cross-sectional (b) TEM and (c) HAADF-STEM images of mesoporous Pd film with vertically-aligned mesochannels. Schematic diagram illustrating the formation of mesoporous Pd film is shown in panel (d). Reproduced with permission.[134] Copyright 2015, American Chemical Society.

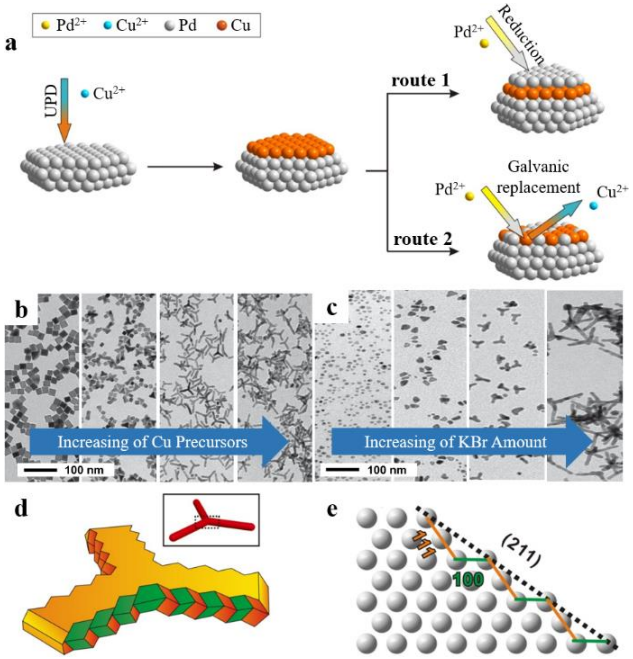

Figure 15. (a) A schematic illustration showing the Cu under potential deposition (UPD) process during the formation of Pd-Cu nanocrystals. TEM images showing the structural variations of the Pd-Cu bimetallic alloy by (b) increasing the amount of Cu precursor (0, 1, 3, and 5 mg, respectively) and (c) increasing the amount of KBr involved in the reaction solution (0, 50, 100, and 300 mg, respectively). (d) A model of the Pd-Cu tripod in the central region marked in the inset, indicating that the side faces are consisted of alternating {100} and {111} steps. (e) An illustration of the atomic arrangement for the side face, showing the alternation of {100} and {111} atom steps. Reproduced with permission.[174] Copyright 2014, Wiley-VCH Verlag GmbH.

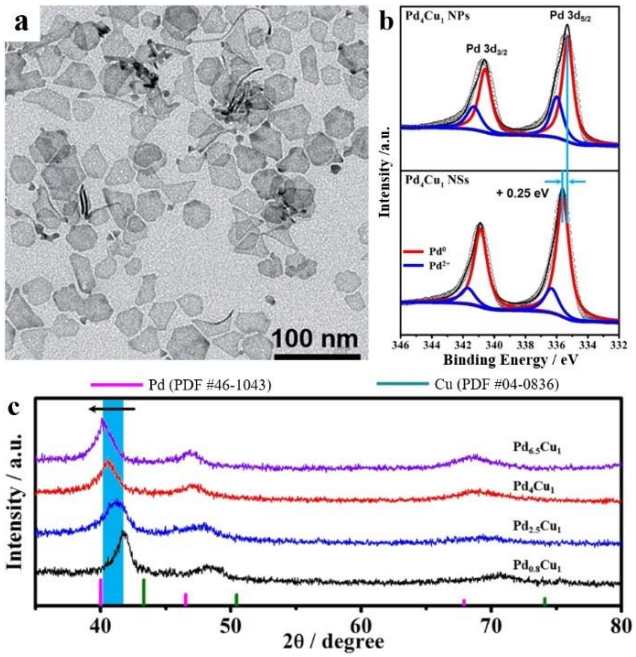

Figure 16. (a) TEM image of Pd_4Cu_1 nanosheets (NSs). (b) The Pd 3d XPS spectra of Pd_4Cu_1 nanoparticles (NPs) and Pd_4Cu_1 NSs. The core-level XPS peak of Pd in Pd_4Cu_1 NSs was shifted by about 0.25 eV toward higher energy compared to that of Pd_4Cu_1 NPs, indicating a down-shift of the *d*-band in Pd_4Cu_1 NSs. (c) X-ray diffraction patterns of PdCu nanostructures obtained with different Pd/Cu ratio. Reproduced with permission.[175] Copyright 2018, The Royal Society of Chemistry.

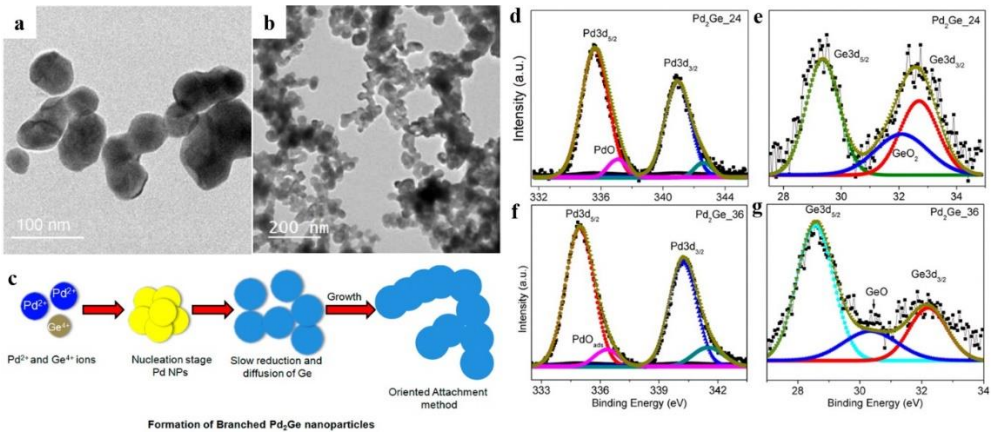

Figure 17. TEM images of (a) Pd_2Ge_24 nanoparticles grown from ellipsoidal particles from small nanoparticles (<15 nm) to smaller joined structures and (b) highly connected network of Pd_2Ge_36 nanoparticles. (c) Mechanism of formation of branched Pd_2Ge nanoparticles by oriented attachment. XPS data of Pd_2Ge_24 and Pd_2Ge_36 for (d, f) Pd3d and (e, g) Ge3d orbitals, respectively. Reproduced with permission.[159] Copyright 2015, The Royal Society of Chemistry.

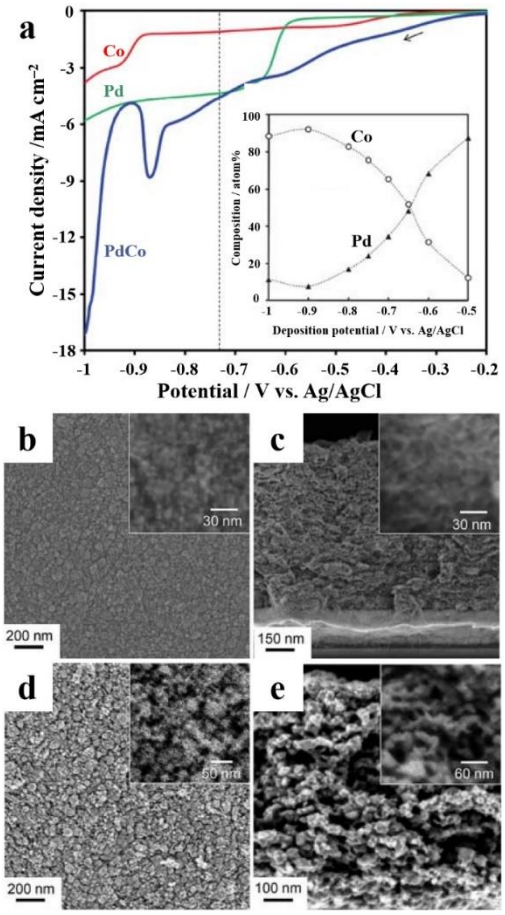

Figure 18. (a) Linear sweep voltammogram (LSV) profiles of mesoporous Co, Pd and PdCo films at 10 mV s^{-1} with a negative scan potential. The vertical dotted line shows the hydrogen evolution potential, 0.73 V *vs.* Ag/AgCl. The inset shows the compositions of the films deposited at different constant potentials (0.5, 0.6, 0.65, 0.7, 0.75, 0.8, 0.9 and 1.0 V vs. Ag/AgCl) for 10 min. (b, d) Top-view and (c, e) cross-sectional SEM images of (b, c) as-deposited and (d, e) de-alloyed mesoporous PdCo films. Reproduced with permission.[164] Copyright 2010, The Royal Society of Chemistry.

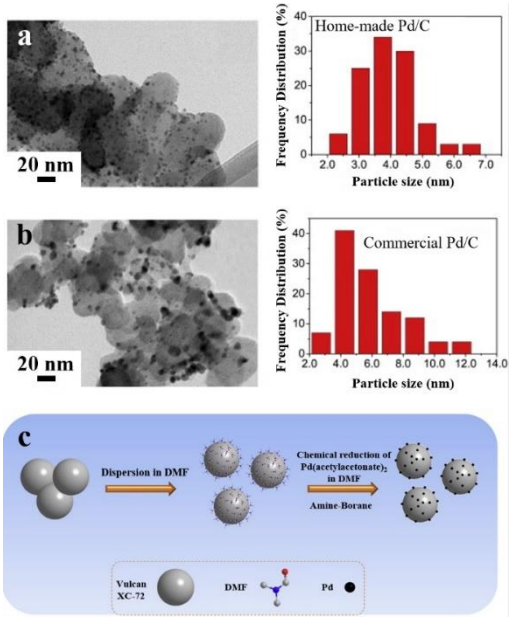

Figure 19. TEM image (left) and particle size distribution histograms (right) of (a) home-made Pd/C and (b) commercial Pd/C catalysts. (c) Schematic illustration of the synthesis process of Pd/C catalyst in DMF. Reproduced with permission.[211] Copyright 2015, Elsevier, Ltd.

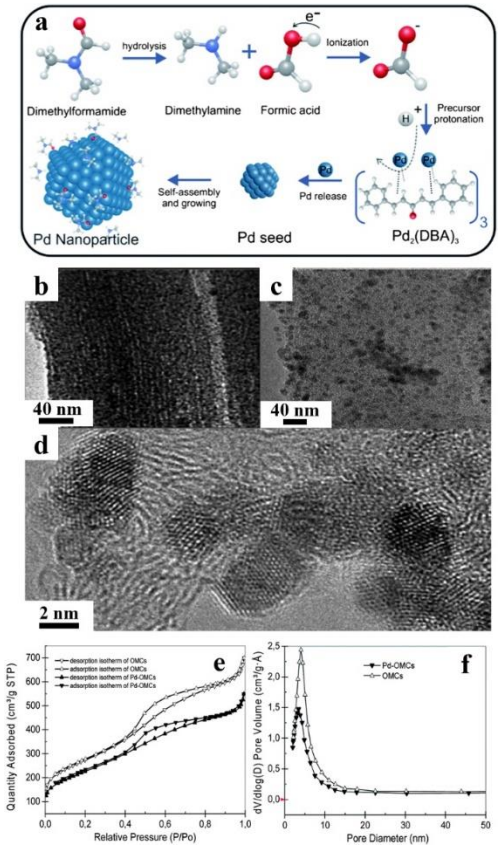

Figure 20. (a) An illustration of the formation mechanism of Pd nanoclusters *via* the decomposition of tri(dibenzylideneacetone)palladium(0), $Pd_2(DBA)_3$, in DMF solution. (b) TEM and (c, d) HRTEM images of Pd–OMCs. (e) Nitrogen adsorption-desorption isotherms and (f) pore size distribution of OMCs (white triangle) and Pd–OMCs (black triangle). Reproduced with permission.[213] Copyright 2014, The Royal Society of Chemistry.

Table 1. Various Pd-based intermetallic and alloy nanocatalysts synthesized through solution-phase and electrochemical deposition methods reported in the literatures.

Compound	Morphology	Intermetallic or Alloy	Synthetic Approach	Features	Applications	Ref.
Pd_2Ge	3D Networks	Intermetallic	Solvothermal	▪ High activity toward ethanol oxidation and better stability compared to Pd/C	Electrooxidation of ethanol	[159]
Pd_3Pb	Nanowire networks	Intermetallic	One-pot reduction	▪ Bifunctional catalyst ▪ Superior long-term stability ▪ Higher activity toward ethanol oxidation and oxygen reduction ▪ Better methanol- and CO-tolerance than PdB	Electrooxidation of methanol and electroreduction of oxygen	[160]
Pd_3Pb	Flower-like nanoparticles	Intermetallic	Polyol method	▪ The synthetic method can be extended for the formation of other Pd and group IV metal-based intermetallics ▪ Higher activity toward ethanol oxidation and formic acid compared to Pd/C	Electrooxidation of formic acid and ethanol	[161]
PdBi	Nanowires	Alloy	Solvothermal	▪ Superior mass activity toward formic acid oxidation in comparison with Pd/C	Electrooxidation of formic acid	[162]
PdCo	Nanoparticles	Alloy	Chemical reduction	▪ Final product composition can be tuned by metal molar ratios ▪ High activity in the order of $Co_{50}Pd_{50}$ > $Co_{60}Pd_{40}$ > $Co_{10}Pd_{90}$ > Pd.	Electrooxidation of formic acid	[163]
PdCo	Mesoporous	Alloy	Electrochemical deposition and de-alloying	▪ Final product composition can be tuned by changing the applied potential deposition ▪ Exhibit higher activity compared to conventional nanoparticle-based catalyst	Electroreduction of oxygen	[164]
PdCo, PdNi	Dendritic	Alloy	One-pot solvothermal	▪ More negative onset potential for CO oxidation ▪ Higher catalytic activity for CO oxidation ▪ High activity toward methanol and ethylene glycol oxidation in the order of PdCo > PdNi > Pd dendritic > PdB	Electrooxidation of methanol and ethylene glycol	[165]
PdCoP	3D Networks	Alloy	Chemical reduction	▪ Large BET surface area ▪ Higher hydrazine oxidation activity than PdCo	Electrooxidation of hydrazine	[166]
PdCu	Branched nanopods	Alloy	Galvanic replacement reaction	▪ More negative onset potential for CO oxidation ▪ High activity toward formic acid oxidation and oxygen reduction ▪ Good stability	Electrooxidation of formic acid Electroreduction of oxygen	[167]
PdCu	Nanowire networks	Alloy	One-pot reduction	▪ High surface area and mass activity toward ethanol oxidation	Electrooxidation of ethanol	[168]
PdCu	Concave tetrahedra	Alloy	One-pot hydrothermal	▪ Stable and tolerance toward CO poisoning ▪ Higher mass activity than PdB toward formic acid oxidation	Electrooxidation of formic acid	[169]
PdCu	Aerogels	Alloy	One-pot reduction	▪ High activity toward ethanol oxidation and better stability compared to Pd/C	Electrooxidation of ethanol	[170]
PdCu	Porous nanoparticles	Alloy	Hydrothermal	▪ High ECSA due to the porous structure ▪ Higher activities for methanol and formic acid oxidation compared to Pd/C ▪ Good stability	Electrooxidation of methanol and formic acid	[171]

PdCu	Hollow nanocubes	Alloy	Solvothermal	▪ High ECSA due to the hollow structure ▪ Higher activity for formic acid oxidation compared to Pd nanoparticles ▪ Good stability	Electrooxidation of formic acid	[172]
PdCu	Nanodendrites	Alloy	Chemical reduction	▪ Tunable Cu to Pd composition ratio ▪ Higher activity and better stability toward methanol oxidation than Pd/C	Electrooxidation of methanol	[173]
PdCu	Nanotripods	Alloy	Chemical reduction	▪ Encased by high-index facets ▪ Mass activity toward formic acid about 8.7 times higher than PdB ▪ Better stability	Electrooxidation of formic acid	[174]
PdCu	Nanosheets	Alloy	Solvothermal	▪ Superior activity about 10 times higher than PdB ▪ Excellent ECSA ▪ Better CO tolerance due to the modulated *d*-band electrons	Electrooxidation of methanol	[175]
PdCu	Spherical, cubic, and dendritic nanoparticles	Alloy	Galvanic replacement reaction	▪ High Faradaic efficiency for CO conversion	Electroreduction of CO_2	[176]
PdCu	3D Branched	Alloy	One-pot reduction	▪ High activity and better stability toward formic acid oxidation compared to PdB and Pd/C	Electrooxidation of formic acid	[177]
PdCuCo, PdCuNi, PdCu	Nanoparticles	Intermetallic	One-pot reduction and thermal annealing	▪ Bifunctional catalyst ▪ Ordered intermetallic phase ▪ Activity increase in the order of Pd/C < Pt/C < ordered PdCu < ordered PdCuNi < ordered PdCuCo	Electrooxidation of ethanol and electroreduction of oxygen	[178]
PdCuCr	Nanoparticles	Alloy	Chemical reduction	▪ Higher activity and selectivity than bimetallic PdCu, PdCr and monometallic Pd	Dehydrogenation of Formic Acid	[179]
PdNi	Nanowire networks	Alloy	Chemical reduction	▪ Higher activity for formic acid oxidation compared to Pd/C ▪ Good stability	Electrooxidation of formic acid	[180]
PdNi	Aerogels	Alloy	One-pot reduction	▪ Superior mass activity toward ethanol oxidation about 5 times higher than Pd/C ▪ Excellent stability	Electrooxidation of ethanol	[181]
PdNi	3D Networks	Alloy	Chemical reduction	▪ Hierarchical pore structure ▪ Superior ORR performance in comparison with PdNi nanoparticles and PdB	Electroreduction of oxygen	[182]
PdNi	3D Networks	Alloy	One-pot reduction	▪ High surface area due to hierarchical porous structure ▪ High activity toward methanol oxidation and better stability compared to Pd/C	Electrooxidation of methanol	[183]
PdNi	Nanowires	Alloy	Electrodeposition	▪ Consist of mesopores (an average diameter of 3-6 nm) ▪ Higher activity for formic acid oxidation compared to Pd/C ▪ Better stability	Electrooxidation of formic acid	[184]
Pd-P	3D Networks	Alloy	Hydrothermal	▪ More negative onset potential for CO oxidation ▪ High activity toward formic acid oxidation and oxygen reduction ▪ Good stability	Electrooxidation of formic acid	[185]
PdPb	Aerogels	Intermetallic	One-pot reduction	▪ Ordered intermetallic phase ▪ Mass activity toward ethylene glycol oxidation about	Electrooxidation of ethylene glycol	[186]

				6 times higher than PdB ▪ Better stability than PdB		
PdSn	Dendritic	Alloy	Electrochemical deposition	▪ More negative onset potential for CO oxidation ▪ Higher catalytic activity for CO oxidation	Electrooxidation of ethanol	[187]
PdTe	Nanowires	Alloy	Hydrothermal	▪ High activity toward ethanol ▪ Mass activity toward ethylene glycol oxidation about 4.5 times higher than Pd/C ▪ Good stability	Electrooxidation of methanol and ethylene glycol	[188]

Biography of Authors

Yusuf Valentino Kaneti obtained his Ph.D. degree in Materials Science and Engineering from the University of New South Wales in 2014. He is currently working as a Research Associate at the I nternational Center for Materials Nanoarchitectonics (MANA)**,** National Institute for Materials Science (NIMS), Japan. His research focuses on the synthesis, characterization and application of porous nanomaterials for energy storage catalysis and gas sensors.

Brian Yuliarto received his master's degree and Ph.D. degree from the University of Tokyo, Japan. He is currently working as a full-time professor at the Department of Engineering Physics, Institute of Technology Bandung, Indonesia. His research focuses on the synthesis and application of metal oxide nanostructures and their composites for gas-sensing, energy and solar cell applications.

P

Yusuke Yamauchi received his B.Eng. degree (2003), M.Eng. degree (2004), and Ph.D. degree (2007) from Waseda University, Japan. After working as a group leader in NIMS, Japan (2007–2016), and a full professor in University of Wollongong, Australia (2016–2017), he joined The University of Queensland, Australia. Currently, he is a full professor at the School of Chemical Engineering and a senior group leader at Australian Institute for Bioengineering and Nanotechnology. He concurrently serves as an honorary group leader of NIMS, and a visiting professor at several universities.

Due to its high catalytic activity, palladium (Pd) has received tremendous attention for many catalytic reactions. Various Pd-based nanoarchitectures, including alloys, intermetallics, and supported Pd materials, have been synthesized through chemical reduction and electrochemical deposition methods to develop costeffective and high-performance Pd-based nanocatalysts.

Keywords: alloys, catalysis, electrochemical deposition, intermetallic structures, palladium nanoarchitectures

Muhammad Iqbal, Yusuf Valentino Kaneti*, Jeonghun Kim, Brian Yuliarto, Yong-Mook Kang, Yoshio Bando, Yoshiyuki Sugahara, and Yusuke Yamauchi*

Chemical Design of Palladium-Based Nanoarchitectures for Catalytic Applications